CHAPTER 16

Photocatalytic Reactor Modeling

FIDERMAN MACHUCA-MARTÍNEZ*[a], MIGUEL ANGEL MUESES*[b], JOSÉ COLINA-MÁRQUEZ*[b], AND GIANLUCA LI PUMA*[c]

[a]Chemical Engineering School, Universidad del Valle, Ciudadela Universitaria de Meléndez, Edif. 336, Cali, Colombia; [b]Chemical Engineering Department, Universidad de Cartagena, Campus de Piedra de Bolívar, Cartagena de Indias, Colombia; [c]Environmental Nanocatalysis & Photoreaction Engineering, Department of Chemical Engineering, Loughborough University, Loughborough, UK LE11 3TU
*E-mail: fiderman.machuca@correounivalle.edu.co, jcolinam@unicartagena.edu.co, mmueses@unicartagena.edu.co, g.lipuma@lboro.ac.uk

16.1 Introduction

The main feature that distinguishes a photoreactor from a chemical reactor is the presence of photons. Photons can be considered as a chemical reagent whose function is that of exciting molecules in homogeneous systems and of generating electron–hole pairs on heterogeneous systems. Consequently, it is of fundamental importance to develop a photocatalytic reactor model that considers the fate of the photons in the reactor.

RSC Energy and Environment Series No. 14
Photocatalysis: Fundamentals and Perspectives
Edited by Jenny Schneider, Detlef Bahnemann, Jinhua Ye, Gianluca Li Puma, and Dionysios D. Dionysiou

Published by the Royal Society of Chemistry, www.rsc.org

The development of a complete photocatalytic reactor model at different scales includes four main methodological components: (i) the reactive system, (ii) the radiation source, (iii) the semiconductor photocatalyst, and (iv) the reactor type and geometry. These elements should be clearly defined to describe correctly the modeling equations and phenomenological processes of a photocatalytic process. In more detail, the mathematical model of the photoreactor includes: mass balances coupled to hydrodynamics equations, reaction rate laws, a quantum yield model and, most importantly, an estimation of the incident radiation field considering a source emission model applicable to either sunlight or artificial light sources, and the formulation of a photon absorption–scattering model which determines the spatial distribution of the "local volumetric rate of photon absorption" (LVRPA) in the reactor (Figure 16.1).

After formulation of the mathematical model, the modeling equations are solved through numerical methods, usually by adjustment of the model parameters and fitting of the model results to the experimental data. The kinetic parameters are usually obtained with optimization algorithms. The numerical solution obtained can then be used to generate simulation data for further experimentation, model validation, and for performing a sensitivity analysis of the model parameters. The scaling-up of the photoreactor to different scales for laboratory, pilot, or industrial applications can finally be developed from the validated model. Figure 16.1 shows a block diagram representing the modeling of a photocatalytic reactor.

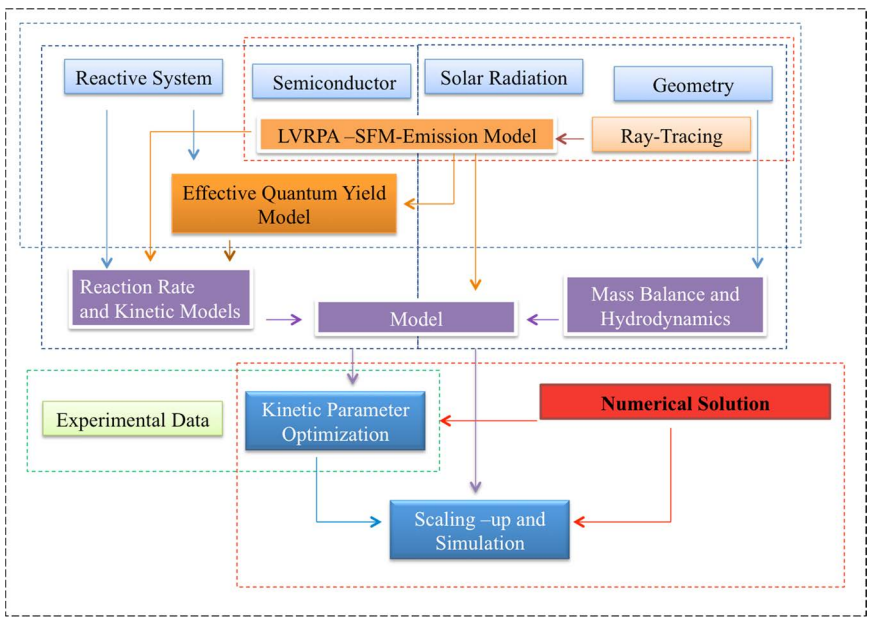

Figure 16.1 Methodological structure for modeling, simulation, and scaling-up of heterogeneous photocatalytic reactors. (Adapted from Mueses *et al.*, 2013.[1] Reproduced with permission of Elsevier copyright 2015.)

16.2 Radiation Field Evaluation

Modeling of the radiation field in a photoreactor involves two generalized sub-models: (i) the photon emission model, which is a mathematical description of the incident radiation to the reactor, from the source (sun light or lamps) to the walls of the photoreactor; (ii) The photon absorption–scattering model, which describes the absorption or scattering of photons in the photoreactor. The two models combined lead to the quantification of the LVRPA in reactors utilizing suspended photocatalysts (*e.g.* powders semiconductors) or the local surface rate of photon absorption (LSRPA) in reactors using immobilized photocatalysts on solid surfaces.

16.3 Emission Model (Lamps)

In most cases, artificial lamps are long slim tubes, which can be mathematically represented in the simplest way by an ideal linear radiation source model. Linear source (LS) models are a mathematical representation of cylindrical lamps in which the ratio of the radius to the length is rather small. When the lamp is considered as a perfect cylinder, extensive source (ES) models can also be used. Table 16.1 summarizes LS and ES models found in the literature.[2]

Cassano and Alfano[3] have critically reviewed the mathematical structures of the above models.

The LSPP model assumes that the cylindrical lamp is a line and all rays emitted by each point of the lamp are located in a plane perpendicular to the lamp at this point. Although this is the simplest light emission model, the limits of this model become apparent since it predicts that the volumetric space not facing the lamps remains in the dark.

The LSSE model is one of the most widely used emission model. It represents the lamp as a line source but retains the three-dimensional nature of

Table 16.1 Radiation emission models for artificial lamps.[2]

Model	Description
LSPP – linear source parallel planes model	Two-dimensional propagation of radiation along parallel planes perpendicular to the center line axis of the lamp
LSSE – linear source spherical emission model	Three-dimensional propagation of radiation with spherical emission
LSDE – linear source diffuse emission model	Three-dimensional propagation of radiation with diffuse emission
ESVE – extensive source volumetric emission model	Three-dimensional source with volumetric emission
ESSE – extensive source superficial emission model	Three-dimensional source with superficial spherical emission
ESDE – extensive source diffuse emission model	Three-dimensional source with superficial diffuse emission

the light propagation. This model is mathematically simple and provides a reasonably good analysis of the radiation field especially in annular photoreactors using lamps with large length/diameter ratios.

The LSDE model was developed to represent the radiation emission from fluorescent lamps. The model assumes that the lamp is a line and that each emitter produces radiation in any direction and in a diffuse way.

The extensive source models, ESVE, ESSE, and the ESDE, consider the three-dimensional nature of energy emission from a radiation source and therefore provide a more realistic representation of most radiant energy sources. The main feature of the ES models is that the lamp is modeled as a volume, thus the lamp radius becomes a design parameter of a photoreactor. However, the application of such models usually results in complex calculations, which in certain cases may not justify the effort of this more rigorous approach.

The ESVE model best represents a UV discharge lamp in which the entire body of the lamp emits radiation in all direction (*e.g.* medium- or low-pressure mercury lamps). The ESSE and the ESDE models fit better to fluorescent lamps. In fluorescent lamps, activated salts coating the walls adsorb the radiation emitted by a small amount of mercury contained inside the lamp. The radiation is then re-emitted by the salts, usually in a continuous wavelength band.[2,3]

16.4 Solar Emission Model

The incident solar radiation is a function of the geographical position on Earth (latitude and longitude) and this is affected by the atmospheric conditions and the season of the year. In tropical countries (*e.g.* Colombia in South America) the incident radiation is effectively invariant all year long, but in other non-equatorial regions (*e.g.* USA or Europe) the incident solar radiation depends on the season of the year.

Table 16.2 shows the incident solar radiation (H) for Cali city, Colombia (3° 30′ North latitude) based on the atmospheric measurement reported by the National Institute of Hydrology, Meteorology and Environmental Studies of Colombia, IDEAM (IDEAM, 2012).

In the work of Colina *et al.*,[4] the UV photon irradiance I_0 to a solar photoreactor was calculated for constant solar radiation along the z axial direction of the reactor (with direct UV radiation between 295 and 384 nm and 4.1% of the total solar radiation), with the total radiation intensity $I_{0,\text{Total}}$ set to 30 W m^{-2}. The ratio between the diffuse radiation and the direct radiation was usually assumed to be constant and set to 75% of the UV transmittance through the clouds. The direct and diffuse radiation components were corrected by the geographical location and season of year, as follows:[4]

$$\frac{I_{0,\text{direct}}}{I_{0,\text{Total}}} = 1 - \frac{I_{0,\text{diff}}}{I_{0,\text{Total}}} = 1 - \frac{4}{3}K_C h_d \tag{16.1}$$

Table 16.2 Solar incident radiation in Cali, Colombia (2012).[4]

Month	H (kW h m^{-2})
January	4.75
February	4.75
March	5.25
April	4.75
May	4.75
June	5.25
July	5.25
August	4.75
September	4.75
October	4.75
November	4.75
December	4.75
Average	4.88

where K_C is the nubosity index with respect to the received radiation H at the location of interest ($K_C = H/H_0$) and h_d is the correction to the diffuse total energy:[1]

$$h_d = 1 - \frac{H_d}{H_0} = \begin{cases} 0.01 \quad \text{for } K_C \le 0.17 \\ -0.188 + 2.272K_C - 9.473K_C^2 + 21.856K_C^3 - 14.648K_C^4 \quad 0.17 < K_C \le 0.80 \end{cases} \tag{16.2}$$

$$H_0 = 24\frac{S}{\pi}E_0\left[h_a - \tan(h_a)\right]\sin(\varphi)\sin(\varpi) \tag{16.3}$$

$$E_0 = 1 + 0.033\cos\eta_{dy} \tag{16.4}$$

$$\varpi = 0.006918 - 0.399912\cos(\eta_{dy}) + 0.070257\sin(\eta_{dy}) - 0.006758\cos(2\eta_{dy}) + 0.000907\sin(2\eta_{dy}) - 0.002697\cos(3\eta_{dy}) + 0.00148\sin(3\eta_{dy}) \tag{16.5}$$

$$\eta_{fy} = \frac{2\pi d_y}{365} \tag{16.6}$$

$$h_a = \arccos(-\tan\varphi\tan\varpi) \tag{16.7}$$

where ϕ is the geographical latitude, η_{fy} is the fraction of the year to the day (d_y) expressed as an angle (example: $d_y = 1$ for January 01), ϖ is the declination angle, and h_a is the solar hour angle. H_0 is the overall solar radiation calculated for a sunny and clear day, E_0 is an eccentricity correction factor, and S is the solar constant (S = 1.367 kW h m^{-2}). Table 16.3 shows the simulation of the solar incident radiation in Cali, Colombia.

Table 16.3 Solar incident radiation in Cali, Colombia (2011). (Adapted from Mueses *et al.*, 2013.[1] Reproduced with permission of Elsevier copyright 2015.).

Month	H (kW h m^{-2})	H_0 (kW h m^{-2})	K_C	H_d/H
January	4.75	9.65150	0.49215	0.61832
February	4.75	10.1292	0.46894	0.66023
March	5.25	10.4566	0.50208	0.59987
April	4.75	10.3768	0.45775	0.67973
May	4.75	9.97681	0.52622	0.55402
June	5.25	9.66041	0.54346	0.52075
July	5.25	9.73505	0.53929	0.52882
August	4.75	10.1042	0.47010	0.65819
September	4.75	10.3604	0.45848	0.67847
October	4.75	10.2041	0.46550	0.66628
November	4.75	9.75572	0.48689	0.62797
December	4.75	9.47154	0.50150	0.60094
Average	4.88	9.99019	0.49270	0.61613

16.5 Photon Absorption–Scattering Model: Evaluation of the Local Volumetric Rate of Photon Absorption, LVRPA

The central aspect in the modeling of a photocatalytic reactor is the calculation of the local volumetric rate of photon absorption (LVRPA) at each point of the reaction space, which requires solving the radiative transfer equation (RTE) in the reaction space.[2] Three methods have been proposed in the literature for calculation of the LVRPA: (1) the "rigorous method" which involves the mathematical solution of the RTE, although its integro-differential nature makes this approach significantly more complex;[3] (2) the "numerical method" which involves the Monte Carlo simulation of the radiation field in the photoreactor, a simple but also a computationally demanding procedure; and (3) the "simplified method" which models the radiation field in the photoreactor using "two-flux" or "six-flux" radiation absorption–scattering models.[5–9]

The rigorous approach advocated by the group of Cassano and Alfano[3] is based on a complete description of the radiation field in the reaction space. The radiative transfer equation in a participating media with absorption and scattering is solved using appropriate boundary conditions, which are dependent on the geometry of the reactor:[10]

$$\frac{\mathrm{d}}{\mathrm{d}s} I_\lambda\left(\vec{x},\vec{\Omega}\right) = -\left[\kappa_\lambda\left(\vec{x}\right) + \sigma_\lambda\left(\vec{x}\right)\right] I_\lambda\left(\vec{x},\vec{\Omega}\right) + \frac{1}{4\pi}\sigma_\lambda\left(\vec{x}\right) \int_{\vec{\Omega}'=4\pi} \rho\left(\Omega' \to \Omega\right) I_\lambda\left(\vec{x},\vec{\Omega}\right) \mathrm{d}\vec{\Omega}' \tag{16.8}$$

Three optical parameters appear in the RTE. These are the spectral volumetric absorption and scattering coefficients (κ_λ and σ_λ) and the scattering phase function $p(\Omega' \to \Omega)$. These depend on the chemical and physical nature

of the catalyst, the particle size, and on the degree of agglomeration of the catalyst in suspension, which is also affected by the degree of mixing. These parameters must be determined in advance with independent experiments in order to compute the radiation field $I_\lambda(\vec{x},t)$ in the reaction space. The LVRPA (Einstein m^{-3} s^{-1}) is then calculated by:[9]

$$\text{LVRPA} = \int_{\lambda_1}^{\lambda_2} \int_{\Omega} \kappa_\lambda I_{\lambda,\Omega}(\vec{x},t) \mathrm{d}\Omega \, \mathrm{d}\lambda \tag{16.9}$$

In the Monte Carlo approach, the RTE is solved by considering a statistically significant number of photons emitted from the radiation source and by following their fate until the photons are either absorbed by the solid photocatalyst or escape from the reactor boundaries as a result of consecutive scattering events. This method is suitable for determining the radiation field in reactors with complex geometries; however, significant computational efforts are often required.[11–13]

Simplified methods for the estimation of the RTE may be suitable for the design and scale-up of photocatalytic reactors. Highly simplified radiation field models such as the zero reflectance model (ZRM) and the two flux model (TFM), although approximate, give an immediate physical understanding of the role played by the key design parameters in photocatalytic reactors.[7,8,14–17] The ZRM is based on the assumption of no photon-scattering by the catalyst particles, while the TFM assumes that photon-scattering can occur in the backward direction only. An extension of the TFM is the "six flux model" (SFM) which has been shown to match quite closely the exact solution of the RTE, while still retaining all the advantages of simplified models.

16.5.1 Two-Flux and Six-Flux Absorption–Scattering Models

The TFM and SFM provide a considerable simplification of the mathematical reactor analysis but yield a sufficiently rigorous representation of the LVRPA in the reaction space. Furthermore, computational time (in terms of readily available personal computers) is significantly reduced from the order of minutes/hours using the Monte Carlo method to seconds or fraction of seconds using the two- and six-flux models. The two most important dimensionless parameters for the modeling of a photocatalytic reactor are the scattering albedo, ω, which characterizes the optical properties of the photocatalyst (the fraction of dispersed energy) and the optical thickness of the reaction space, τ, which is a measure of the degree of opacity of the photoreactor.[18]

The scattering albedo is defined as:[19]

$$\omega = \frac{\sigma}{\kappa + \sigma} \tag{16.10}$$

where σ and κ are the specific mass scattering and absorption coefficients of the photocatalyst suspension. As these are wavelength-dependent quantities, the following analysis refers to monochromatic irradiation (*e.g.* UVC radiation sources). However, with polychromatic radiation sources (*e.g.* in

solar applications or with UVA radiation sources)[1,16,18] σ and κ may be estimated as their average over the useful spectrum of the incident radiation:

$$\sigma = \frac{\int_{\lambda_{min}}^{\lambda_{max}} \sigma_\lambda I_\lambda d_\lambda}{\int_{\lambda_{min}}^{\lambda_{max}} I_\lambda d_\lambda} \tag{16.11}$$

$$\kappa = \frac{\int_{\lambda_{min}}^{\lambda_{max}} \kappa_\lambda I_\lambda d_\lambda}{\int_{\lambda_{min}}^{\lambda_{max}} \kappa_\lambda d_\lambda} \tag{16.12}$$

where λ_{min} and λ_{max} are, respectively, the minimum and maximum wavelengths of the incident radiation that can be absorbed by the photocatalyst. The averaged quantities should be used with caution as this is not a completely rigorous approach and may lead to errors, if the radiation emission spectra of the lamp is irregular. The scattering albedo should be evaluated using the absorption and scattering coefficients determined experimentally under the prevailing conditions of the slurry suspension (*i.e.* with the observed degree of agglomeration of photocatalyst in the suspension; *cf.* earlier discussion on the effect of catalyst particle size).[19]

The optical thickness τ of the photocatalytic reactor is a function of the extinction coefficient ($\sigma + \kappa$) of the suspension, the thickness of the reaction space (δ) and the concentration of photocatalyst (c_{cat}). The physical meaning of the optical thickness is the ratio of the depth of the reaction space divided by the photons mean free path in the suspension. The experimental methods used to measure the extinction coefficient ($\sigma + \kappa$) and the scattering albedo (ω) have been reported in the literature:[18]

$$\tau = (\sigma + \kappa) c_{cat} \delta \tag{16.13}$$

To a large extent, the scattering properties of the photocatalyst and the geometrical configuration of the photoreactor determine the degree of complexity of a mathematical model.

Figure 16.2 shows a schematic representation of a double flat-plate reactor of thickness $d = H_R$, located perpendicular to the source. Additionally, it presents a profile of LVRPA on the y-coordinate, with the maximum value at the interface surface-flow ($LVRPA_s$), and the minimum value at reactor bottom ($LVPRA_\infty$).

The region where there is a gradient of energy absorption is the "boundary layer of photon absorption", and its thickness, δ_{abs}, is defined as the y-value that satisfies the following ratio:[16]

$$\frac{LVRPA_s - LVRPA_{\delta abs}}{LVRPA_s - LVRPA_\infty} = 0.99 \tag{16.14}$$

This definition of boundary layer thickness for the absorption of radiant energy is analogous to the definition in transport phenomena of the

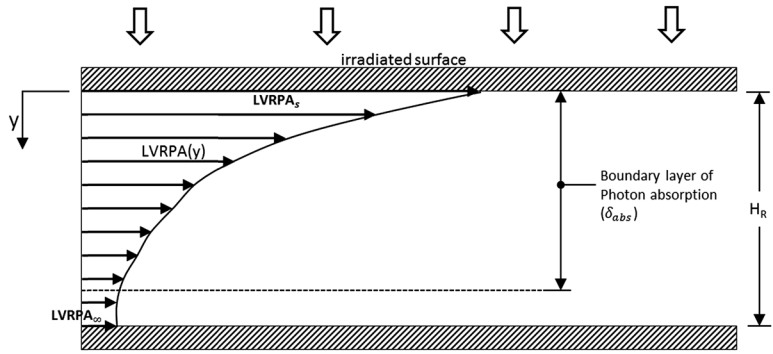

Figure 16.2 Boundary layer of photon absorption in a double flat-plate reactor irradiated onto an upper plate. (Adapted from Otálvaro-Marín *et al.*, 2014.[16])

thicknesses for hydrodynamic, thermal, and concentration boundary layers on a flat plate. The δ_{abs} can be understood as the reactor thickness measured from the irradiated surface, where 99% of total energy is absorbed. For this reason, the boundary layer thickness becomes a design parameter, which determines the optimum thickness of flat-plate or annular reactors. Oversizing the photoreactor thickness can lead to the presence of a dark sub-layer, where there is no considerable rate of photon absorption.

This design parameter is similar to the apparent optical thickness used for sizing annular reactors and solar compound parabolic collectors (CPCs).[9,15,17,18] The δ_{abs} uses the analogous concept of boundary layer thickness to obtain optimal light absorption in the reactor and depends on the nature and the concentration loading of the photocatalyst.

The SFM can be used to model the radiation field in a reactor irradiated with solar light. The LVRPA divided by the flux of incident radiant energy in the reactor (I_0) expressed by this model is:

$$\mathrm{LVRPA} = \frac{I_0}{\lambda_{\omega,\mathrm{corr}}\omega_{\mathrm{corr}}(1-\gamma)}\left[\left(\omega_{\mathrm{corr}} - 1 + \sqrt{1-\omega_{\mathrm{corr}}^2}\right)e^{-r_p'/\lambda_{\omega,\mathrm{corr}}} + \gamma\left(\omega_{\mathrm{corr}} - 1 - \sqrt{1-\omega_{\mathrm{corr}}^2}\right)e^{r_p'/\lambda_{\omega,\mathrm{corr}}}\right] \tag{16.15}$$

where r_p is the photon coordinate, $r_p = y$ in a flat-plate reactor, ω_{corr} is the corrected scattering albedo, $\lambda_{\omega,\mathrm{corr}}$ corresponds to the corrected value of mean free path of photons in the suspension and γ is a SFM parameter.[1,16]

The scattering albedo ω requires a correction (ω_{corr}) in the SFM, which is a function of the probabilities of forward, backward, and sideways scattering (p_f, p_b and p_s):[12,14,17–19]

$$\omega_{\mathrm{corr}} = \frac{b}{a} \tag{16.16}$$

where:

$$a = 1 - \omega p_f - \frac{4\omega^2 {p_s}^2}{1 - \omega p_f - \omega p_b - 2\omega p_s} \tag{16.17}$$

$$b = \omega p_b - \frac{4\omega^2 p_s^2}{1 - \omega p_f - \omega p_b - 2\omega p_s} \tag{16.18}$$

The probabilities p_f, p_b, and p_s equal 0.11, 0.71, and 0.045, respectively, for a phase function of large sphere with diffuse reflectance.[7,8,12] The mean free path of photons in the suspension (λ_0) and its corrected value ($\lambda_{\omega,corr}$), are a function of the catalyst concentration as shown by Li Puma *et al.*[17,18]

16.6 Application of SFM in Flat-Plate Photoreactors

Figure 16.3 shows the LVRPA/I_0 profiles as a function of y-coordinate in a flat-plate photoreactor (H_R = 1 cm) irradiated with solar radiation, which uses suspended Degussa and Aldrich photocatalysts powders at different catalyst concentrations. The dimensionless optical thickness ($\tau = H_R/\lambda_0$) in these simulations varies from 4 to 22 depending on loading and type of catalyst.[16,17]

The LVRPA/I_0 at the irradiated surface of the reactor increases with catalyst concentration due to the contribution arising from back-scattered photons by the subsequent layers of catalyst inside the reactor. As a consequence, the rate of photon absorption is significantly higher than the value calculated using the incident photon flux. The profile of LVRPA/I_0 with respect to the y-coordinate is a function of the extinction coefficient ($\sigma + \kappa$) and therefore the optical thickness, τ. Figure 16.3 shows that the total photonic energy absorbed in the system diminishes rapidly as the catalyst concentration is increased and at higher values of the extinction coefficient.

The distance from the surface ($y = 0$) where the radiant energy is effectively absorbed (boundary layer of photon absorption) also depends on the concentration and type of catalyst. For catalyst loading greater than 0.3 g L^{-1}, the LVRPA/I_0 at the back wall of the reactor is insignificant.

Figure 16.4 shows the VRPA/I_0 profiles (as solid lines) as a function of catalyst loading inside a flat-plate reactor, for six different commercial brands of TiO_2 catalysts. For all catalysts, the rate of photon absorption is small when the loading is less than 0.2 g L^{-1}; from 0.2 to 0.4 g L^{-1} higher values of VRPA/I_0 are obtained, approaching the optimal operating conditions for this system; and at loadings greater than 0.4 g L^{-1} a saturation condition is reached implying that further increases in catalyst concentration become irrelevant.

The profile of the VRPA/I_0 in Figure 16.4 further shows that the absorption of radiant energy is higher in catalysts with lower scattering albedos, which means that high absorption coefficients and low scattering coefficients result in a greater rater of photon absorption. The capacity to absorb energy by the commercial TiO_2 catalyst follows the order: Fluka > Fischer > Merck > Aldrich > Degussa P25 > Hombikat.

The Aldrich catalyst has a maximum VRPA, which is 7% higher than the value with the Degussa catalyst. Another study performed with polychromatic

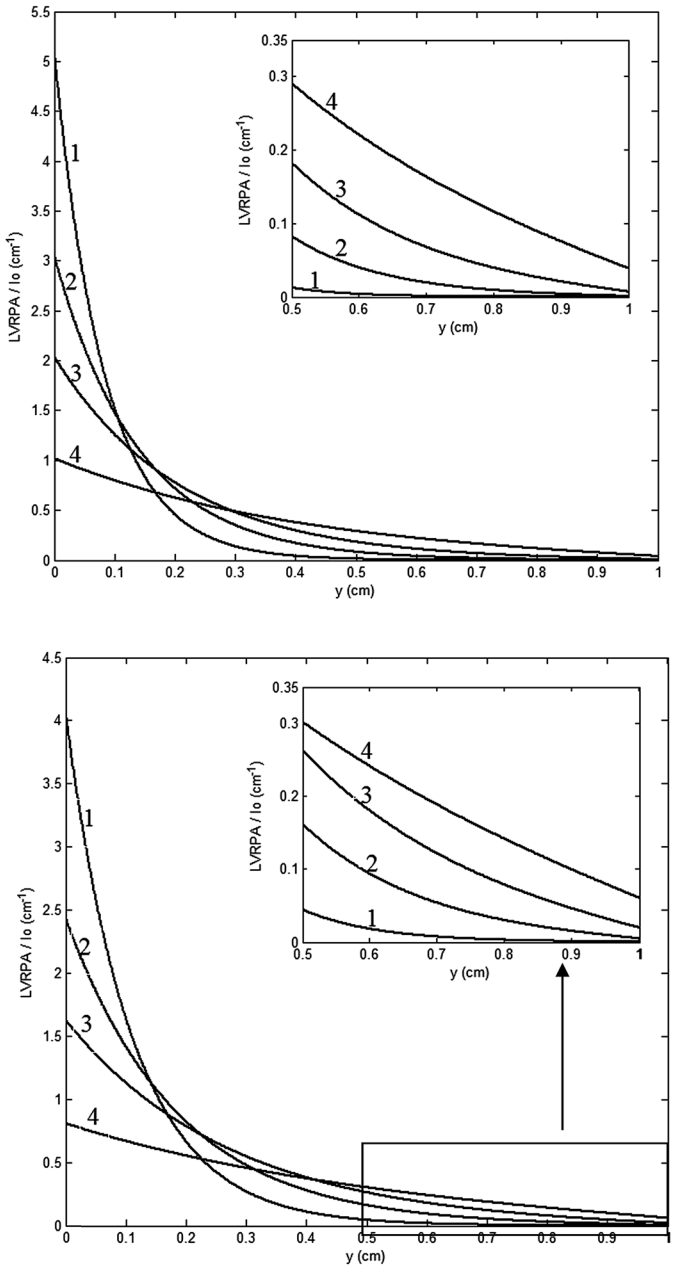

Figure 16.3 Profile of energy absorption rate (LVRPA/I_0) through a fluid (y-coordinate) for Degussa P25 (upper) and Aldrich (lower) catalysts. Catalysts loading (g L^{-1}): line 1 = 0.5, line 2 = 0.3, line 3 = 0.2, and line 4 = 0.1.[16]

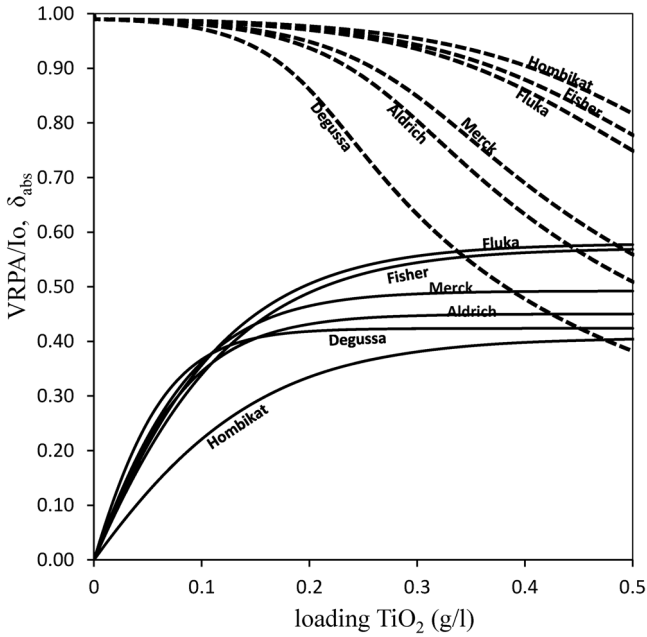

Figure 16.4 VRPA and boundary layer thickness of photon absorption of a flat-plate solar photoreactor for different commercial TiO_2 as a function of its loading. VRPA/I_o (—); δ_{abs} (-----).[16]

radiation, using UV lamps, showed the Aldrich catalyst to be 19% more efficient than Degussa P25.[13]

16.7 Application of SFM in Solar CPC and FPR Reactors

The SFM is particularly suitable for estimating LVRPA profiles in CPC and FTR solar photoreactors.[1,18] The main challenge in the modeling of these photoreactors is the evaluation of the radiation reflected by the collectors that reaches the reactor wall. For this purpose the ray-tracing technique combined with the mathematical expressions of the solar radiation emission model can be used to estimate the fraction of reflected UV solar light that reaches the reactor wall. Using the SFM parameters (Table 16.4) and the solar radiation conditions for Cali, Colombia (IDEAM 2012, ASTM 2008)[18] on a clear and sunny day with I_0 = 30 W h m^{-2} as the standard, the LVRPA profiles in CPCs and flat-plate reactors (FPR) were evaluated as shown in Figure 16.5.

The distribution of the LVRPA shows that, in both geometries, there is a high rate of photon absorption at the reactor boundary layer near the wall. In this example, the high value of optical thickness of the suspension enhances the shielding effects and as a result the deep regions in the reactors are not being illuminated.

Table 16.4 SFM optical parameters.

Parameter	Value
Specific mass absorption coefficient, κ ($m^2\ kg^{-1}$)	174.745
Specific mass scattering coefficient, σ ($m^2\ kg^{-1}$)	1295.749
Scattering albedo, ω (dimensionless)	0.8812
SFM parameter, a_{SFM} (dimensionless)	0.8734
SFM parameter, b_{SFM} (dimensionless)	0.6546
Scattering corrected albedo, ω_{corr} (dimensionless)	0.7496

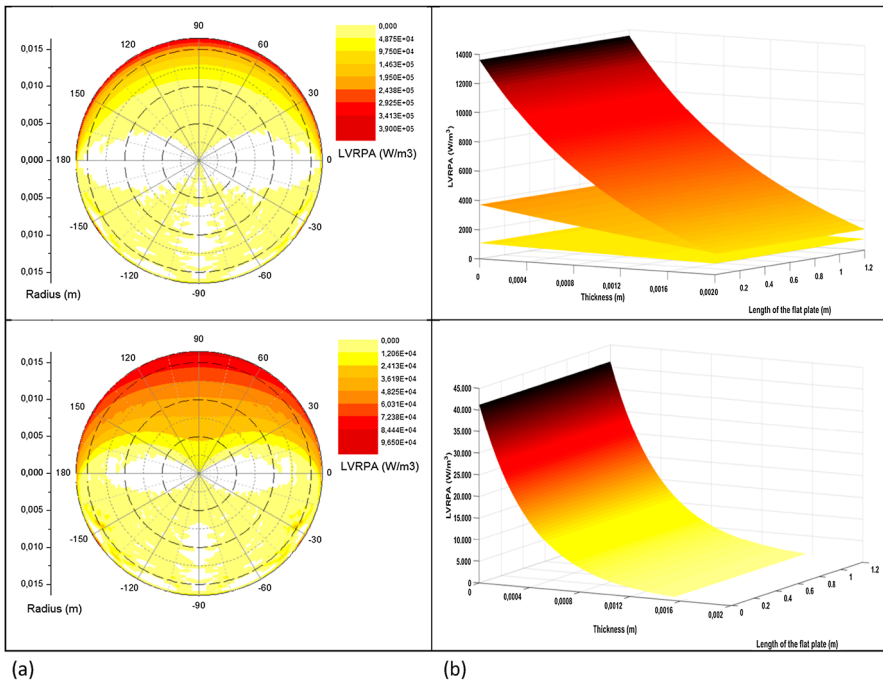

Figure 16.5 Radiation field simulation with SFM: (a) CPC-I (top) C_{Cat} = 0.3 g L^{-1}; (bottom) C_{Cat} = 0.5 g L^{-1}. (b) FPR (top) C_{Cat} = 1.0, 0.3, and 0.01 g L^{-1}; (bottom) C_{Cat} = 3.5 g L^{-1}.

Figure 16.6 shows the overall rate of energy (photon) absorption (OVREA), the integration of the LVRPA over the volume of the reactor, in a CPC and a FPR as a function of catalyst loading and for different values of the scattering albedo. At high catalyst loadings, the OVREA in the FPR (optical path-length 1.6 mm) approaches saturation values since the reactor optical thickness becomes very large.

For the FPR, the increase in catalyst concentration raises the amount of energy absorbed in the reactor. The absolute values of the OVREA for FPR are much higher than the values for the CPC, regardless of the values of the scattering albedo. The effect of the radiation scattering is significant in the two

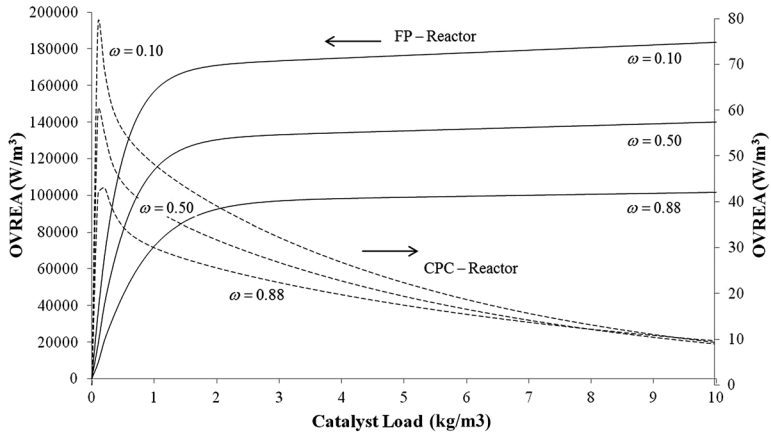

Figure 16.6 Effects of the catalyst load and scattering albedo on the overall volumetric rate of energy absorption (OVREA); FPR (dashed line); CPC-I (solid line).[1] (Adapted from Mueses *et al.*, 2013.[1] Reproduced with permission of Elsevier copyright 2015.)

reactors; however, the numerical values of the OVREA differ by up to three orders of magnitude between the FPR and the CPC due to the much smaller volume of the FPR in comparison to the CPC.

16.8 Photocatalytic Reaction Kinetics Model

The design of solar reactors requires an evaluation of the dynamics of molecular processes at the semiconductor/solution interface. The main limitation is usually the formulation of a detailed mechanism of the photocatalytic process (both physical phenomena and chemical reactions) involving complex substances or mixtures. In general, the initial reaction steps are well understood including the generation of photogenerated electron–hole pairs, their recombination and the capture and transport of these *via* charge carrier species adsorbed on the catalyst surface (water molecules, molecular oxygen, and hydroxyl ions). The trapping of charges by the carrier results in the generation of hydroxyl and peroxyl radical species which may subsequent attack substrate molecules $[R_i]$ through redox reactions.[20–26] Controversies exist regarding the redox reactions, both in terms of the activation mechanism, as well as the spatial location at the interface semiconductor/solution in which photo-oxidation reactions take place.[25,26] For the activation mechanisms, the photogenerated free holes (h_f^+) may react directly with organic substrates by direct hole transfer. Alternatively, the oxidation of substrates may occur by indirect transfer of photogenerated $^{\bullet}OH$ radicals (surface voids of trapped h_s^+).[23,26] The oxidation reactions can also occur in the space-charge region of the catalyst (Stern superficial plane) by direct hydroxyl radical attack on the molecules of the organic compounds adsorbed on the surface (direct attack, where the molecular adsorption of reactive species is the process limiting the

reaction rate).[27–31] The direct hydroxyl radical attack may occur at the Helmholtz boundary layer. In this case, molecular adsorption is not required since the photogenerated $^{\bullet}OH$ may diffuse into the solution to attack the organic species. Since the second-order rate constant of $^{\bullet}OH$ attack on organic species is very large (order of 10^9 mol s^{-1}) molecular diffusion of organic species is in this last case the rate-limiting step.[30]

These discrepancies have led to the proposal of different empirical and semi-empirical kinetic models, which describe the photocatalytic degradation of organic pollutants.[32–38] A very large number of studies in the literature report that the photo-oxidation rates of species follow an apparent pseudo-Langmuir–Hinshelwood (L–H) mechanism, implicitly assuming that adsorption–desorption equilibrium occurs not only in the dark but also during irradiation. Typically, a correction factor associated with the intensity of the incident luminous flux is used to multiply the L–H equation. Although the numerical predictions of experimental data are adequate in most cases, the model in its original form is an equilibrium model and is therefore unable to describe the system dynamics at high substrate concentrations and at acidic pH (highly charged surfaces), which makes the L–H model undesirable because the process of photocatalysis with TiO_2 is favored at low pH.[23] Despite the controversies, a global approach can be used to describe the photodegradation of organic substances in the presence of suspended TiO_2.[21,24,39] Turchi and Ollis (1990) proposed a mechanism based on photogenerated hydroxyl radical attack (Table 16.5).[25] In this mechanism, the main reaction

Table 16.5 Reaction scheme for the photogeneration of hydroxyl radical.[25] (Adapted from Mueses *et al.*, 2013.[1] Reproduced with permission of Elsevier copyright 2015.).

Step	Reaction	
Activation	$TiO_2 + h\nu \rightarrow e^-_{BC} + h^+_{BV}$	(T1)
Adsorption	$O^{2-}_L + Ti^{IV} + H_2O \leftrightarrow O_LH^- + Ti^{IV}\bullet OH^-$	(T2a)
	$Ti^{IV} + H_2O \leftrightarrow Ti^{IV}\bullet H_2O$	(T2b)
	$Site + R_i \leftrightarrow R_{i,ads}$	(T3)
	$OH^{\bullet} + Ti^{IV} \leftrightarrow Ti^{IV}\bullet OH^{\bullet}$	(T4)
Recombination	$e^- + h \rightarrow heat$	(T5)
Hole trapping	$Ti^{IV}\bullet OH^- + h^+ \rightarrow Ti^{IV}\bullet OH^{\bullet}$	(T6a)
	$Ti^{IV}\bullet H_2O + h^+ \leftrightarrow Ti^{IV}\bullet OH^{\bullet} + H^+$	(T6b)
	$R_{i,ads} + h^+ \leftrightarrow R^+_{i,ads}$	(T7)
Electron trapping	$Ti^{IV} + e^- \leftrightarrow Ti^{III}$	(T8a)
	$Ti^{III} + O_2 \leftrightarrow Ti^{IV}\bullet O_2^-$	(T8b)
Hydroxyl attack	$Ti^{IV}\bullet OH^{\bullet} + R_{i,ads} \rightarrow Ti^{IV} + R_{j,ads}$	(T9)
	$OH^{\bullet} + R_{i,ads} \rightarrow Ti^{IV} + R_{j.ads}$	(T10)
	$Ti^{IV}\bullet OH^{\bullet} + R_i \rightarrow Ti^{IV} + R_j$	(T11)
	$OH^{\bullet} + R_i \rightarrow Ti^{IV} + R_j$	(T12)

pathway is oxidation due to the cleavage of carbon–hydrogen bonds induced by hydroxyl radicals generated from charge transfer to the semiconductor holes (h^+) by adsorbed species (hydroxyl ions or water molecules). Hydroxyl radicals can interact with the solid through irreversible reactions, react with organic substances in the adsorbed state, or migrate to the interface within the Helmholtz plane and react with free organic molecules at the interface.

In this approach, the trapped holes are considered predominant in reactions involving hydroxyl ions or adsorbed water molecules. Instead holes trapped by organic molecules are considered to have low reactivity. Finally, the capture of the photogenerated electrons occurs due to the interaction of the active sites of the solid with the oxidant (molecular oxygen) forming superoxide ions.

Alfano, Cabrera, and Cassano (1997)[24] formulated a mathematical model from the mechanism of Turchi and Ollis (1990), considering the concentrations of hydroxyl ions and water to be nearly constant in the system and assuming that recombination processes occur at the Stern surface plane of the particle.[32] The concentrations of photogenerated electrons and holes were also assumed to be equal. Under these assumptions, the contaminant reaction rate law on a catalyst particle suspended in a photocatalytic system is given by:[24]

$$-r_{\mathrm{P}} = \alpha_1^{'}\left\{\left(\frac{E\left(R_i,R_j\right)}{1+E\left(R_i,R_j\right)}\right) - \sqrt{\left(\frac{E\left(R_i,R_j\right)}{1+E\left(R_i,R_j\right)}\right)^2 + \frac{\alpha_2^{'}}{C_{\mathrm{Cat}}}\int_{\lambda} e_{\lambda}^{\mathrm{a}}\,\mathrm{d}\lambda}\right\}\alpha_{3,i}\frac{[R_i]}{\left(1+E\left(R_i,R_j\right)\right)} \tag{16.19}$$

$$\alpha' = \frac{\left(k_6^{'} + a_{\mathrm{S}}\right)^2}{2k_{\mathrm{s}}\upsilon_{\mathrm{P}}} \tag{16.20}$$

The model was applied and successfully validated for the photodegradation of trichloroethylene.[24] However, the quantum yield dependence of the rate was removed by the term α'_2 and considered a global constant in this model.

The quantum yield for heterogeneous systems is the quotient of the local reaction rate in the reactor and the local volumetric rate of photon absorption (LVRPA).[40] Reaction models that explicitly express the rate in terms of quantum yields make use of adjustable model parameters in the reaction rate law, which are assumed constants in the specific system and independent of operating conditions other than the photon irradiance. However, it has been shown that the process conditions (initial concentration, pH, catalyst load), the type of reactor, the scale of operation, and type of catalyst affect the overall contaminant degradation quantum yields.[41,42]

From Ollis' mechanism,[25] it is possible to establish a generalized model that predicts the degradation of organic substances by means of solar photocatalysis using suspended TiO_2–P25. This generalized model works as the

coupling of a modified reaction rate kinetic equation, which includes the L–H model, and a new model of "effective" quantum yield based explicitly on the optical properties of the semiconductors photocatalyst, hence, on the incident irradiance, but independent of the chemical nature of the reactive system. This model can be used for the scaling, modeling, and simulation of solar photoreactors. In this model, the solar radiation field and the absorption of radiation were described using the SFM and the ray tracing technique, models that satisfactorily quantify the performance of large-scale solar photocatalytic reactors.[43–46]

The kinetic equation proposed by Alfano, Cabrera, and Cassano (1997) has $N + 2$ adjustable parameters.[24] The equation has a mathematical structure that includes the L–H model and, according to its authors, corresponds to a modification of that model. This condition implies a high adsorption of dissociated water molecules at the Stern plane.[47,48] In this way, assuming that the concentration of water molecules and hydroxyl ions adsorbed on the surface is kept constant at any one time and that, within the solar scale, the molecular process of adsorption of organic substrates is slow due to the effects of times of operation, it is possible to consider that $E(R_i, R_j) \gg 1$.[49] The reaction rate per photocatalytic particle can therefore be rewritten as follows:[1,24]

$$-r_P = \alpha_1' \left\{ -1 + \sqrt{1 + \frac{2}{\alpha_1'} R_g} \right\} \alpha_{3,i} \frac{[R_i]}{\left(1 + E\left(R_i, R_j\right)\right)} \tag{16.21}$$

$$E\left(R_i, R_j\right) = \sum_{k=1}^{N} \alpha_{3,k}\left[R_k\right] = \alpha_{3,i}[R_i] + \sum_{\substack{j=1 \\ j \neq i}}^{Nc} \alpha_{3,j}[R_j] \tag{16.22}$$

The above expression possesses a mathematical structure associated with the L–H model. However, this equation can be generalized and applied to different reaction systems since the correction factor $\left(-1 + \sqrt{1 + 2R_g / a_1'}\right)$ incorporates the effects of photon irradiance, catalyst loading, and quantum yield (within the R_g term) and is uncoupled from the L–H term.

Summing up the reaction rates per particle over all the N_V particles suspended in the solution volume yields the reaction rate equation for the ith component in solution:[1]

$$r_i = \nu_i \frac{S_g}{a_S} C_{Cat} \alpha_1' \left\{ -1 + \sqrt{1 + \frac{2}{\alpha_1'} R_g} \right\} \frac{\alpha_{3,i}\left[R_i\right]}{1 + E\left(R_i, R_j\right)} \tag{16.23}$$

where S_g is the catalyst-specific surface ($m^3\ kg^{-1}$), C_{Cat} is the catalyst concentration, a_S is the area per volume of suspension, r_i (mol $m^{-3}\ s^{-1}$), and R_g is the initial electron–hole generation rate.

For a heterogeneous system, the range of generation of electron–hole couples (Table 16.5) from N_V irradiated catalyst particles contained in the volume

υ_R is given by eqn (16.24) in which the electron–hole pairs are assumed to be generated with a primary quantum yield (Φ_λ):

$$R_g = \frac{1}{N_V}\int_\lambda \Phi_\lambda \hat{e}^a_\lambda \, d\lambda \tag{16.24}$$

$$N_V = \frac{C_{Cat}}{\upsilon_P \rho_P} \tag{16.25}$$

where $\hat{e}^a{}_\lambda$ is the total volumetric absorption rate of photons (LVRPA, Einstein m^{-3} s^{-1}) and υ_P and ρ_P are the volume and catalyst particle densities, respectively. Here, radiation absorption is considered a volumetric phenomenon that occurs at the irradiated semiconductor surface, and absorption occurs only at the catalyst particles.

The case of solar radiation requires the modification of eqn (16.26), taking the parameter R_g and generalizing it for the case of overall integrated polychromatic radiation:[1]

$$R_g = \frac{\upsilon_P \rho_P}{C_{Cat}} \Phi_g \hat{E}^a_{g(\lambda \to \lambda')} \tag{16.26}$$

$$\Phi_g = \frac{\int_\lambda \Phi_\lambda \hat{e}^a_\lambda \, d\lambda}{\int_\lambda \hat{e}^a_\lambda \, d\lambda} \tag{16.27}$$

$$\hat{E}^a_{g(\lambda \to \lambda')} = \frac{\int_\lambda \hat{e}^a_\lambda I_\lambda \, d\lambda}{\int_\lambda I_\lambda \, d\lambda} \tag{16.28}$$

where Φ_g is the overall effective quantum yield of the process (EGQY) and $\hat{E}^a_{g(\lambda \to \lambda')}$ is the overall volumetric rate of energy absorption of OVREA. The approximation of constant global parameters is valid only if pseudo-isotropic systems are considered, where the properties are calculated as functions of integrated variational parameters.[44]

16.9 Generalized Model

When introducing the global parameters (quantum yield and LVRPA) into the new reaction rate equation and assuming that the reaction is referred only to the primary water contaminant of interest, then $[R_i] = c_i$; $\nu_i = -1$; $E(R_i, R_j) = \alpha_{3,i} c_i$; $\alpha_1 = \alpha'_1/a_S$; $\alpha_{3,I} = k_A^{L-H}$; $\alpha_2 = 1/\alpha_1$; where the particle constant κ_P is given by:[1]

$$\kappa_P \equiv \frac{2}{S_g C_{Cat}} \tag{16.29}$$

The reaction rate equation for heterogeneous photocatalytic degradation in arbitrary suspended semiconductor substrates (with simple or complex

multicomponent systems, such as mixtures, pesticides, dyes, wastewater, *etc.*) is given by:[1]

$$r_i = -2\frac{\alpha_1}{\kappa_P}\left[-1+\sqrt{1+\frac{\kappa_P}{\alpha_1}\Phi_g\hat{E}^a_{g(\lambda\to\lambda')}}\right]\theta_i^{L-H} \tag{16.30}$$

with:

$$\theta_i^{L-H} = \frac{k_A^{L-H}c_i}{1+k_A^{L-H}c_i} \tag{16.31}$$

Eqn (16.30) is the L–H kinetic expression, with reaction rate r_i (mol m^{-3} s^{-1}), surface area per mass of catalyst S_g (m^2 kg^{-1}), catalyst load C_{Cat} (kg m^{-3}), substrate concentration c_i (mol m^{-3}), particle constant κ_P (m^3 m^{-2}), effective overall quantum yield Φ_g (mol Einstein^{-1}), overall volumetric rate of energy absorption $\hat{E}^a_{g(\lambda\to\lambda')}$ (Einstein m^{-3} s^{-1}), an L–H type of kinetic constant $k^{L-H}{}_A$ (m^3 mol^{-1}) and a reaction kinetics rate constant α_1 (mol m^{-2} s^{-1}). The proposed model has two adjustable parameters (α_1 and $k^{L-H}{}_A$), provided that the overall quantum yield is a function independent of the reaction rate data. The above model allows for some simplifications that result in expressions usually used in processes of photodegradation of organic compounds. Table 16.6 summarizes these approximations.

Table 16.6 Simplifications to the proposed model. (Adapted from Mueses *et al.*, 2013.[1] Reproduced with permission of Elsevier copyright 2015.).

Case	Conditions	Modified model
I. $1 \gg \frac{\kappa_P}{\alpha_1}\Phi_g\hat{E}^a_{g(\lambda\to\lambda')}$	The overall reaction rate controls the process.	$r_i = -K_{Kin}\hat{E}^a_{g(\lambda\to\lambda')}\theta_i^{L-H}$
	$\sqrt{1+\frac{\kappa_P}{\alpha_1}\Phi_g\hat{E}^a_{g(\lambda\to\lambda')}} = 1+\frac{1}{2}\frac{\kappa_P}{\alpha_1}\Phi_g\hat{E}^a_{g(\lambda\to\lambda')}$	Direct dependency on photon flux[32]
II. $1 \ll \sqrt{\frac{\kappa_P}{\alpha_1}\Phi_g\hat{E}^a_{g(\lambda\to\lambda')}}$	System with lowest reaction rate (first order) and high dependency on photon flux	$r_i = -K_{Kin}\sqrt{\hat{E}^a_{g(\lambda\to\lambda')}}\frac{k_A^{L-H}c_i}{1+k_A^{L-H}c_{i,0}}$
		L–H model is obtained with root square of LVRPA[45]
III. $k_A^{L-H} \gg 1$	Diffusion controls the process	$r_i = -K_{Kin}\sqrt{\hat{E}^a_{g(\lambda\to\lambda')}}$
		Reaction rate is independent of initial concentration of substrate and depends only on the photon flux[32,36–38]
IV. $1 \gg E(R_i, R_j)$	Systems with high molecular adsorption	$r_i = -2\frac{\alpha_1}{\kappa_P}\left[-1+\sqrt{1+\alpha_2\hat{E}^a_{g(\lambda\to\lambda')}}\right]c_i$
		Model with correction factor based in LVRPA, a constant global and first order[33,38]

Further to the reaction rate law and radiation field model, a material balance and a hydrodynamic model applied to the solar photoreactor need to be considered. The material balance for a recycle type batch photoreactor is:

$$\frac{\partial}{\partial t} c_i(t) = \left(\frac{\upsilon_R}{\upsilon_T}\right) \left\langle R_i \right\rangle_R (t) \tag{16.32}$$

where $c_i(t)$ is the overall concentration of the ith contaminant that changes with time, $<R_i>$ is the average reaction rate in the reactor, and υ_R and υ_T are the reaction volume (exposed to radiation) and the total reaction volume of the system (reactor plus recycle), respectively.

Since the incident solar radiation varies over time due to the effect of atmospheric variations, geographical location, and seasonal period, a standardized treatment time (t_{30W}) is usually employed, which corresponds to the average standard radiation irradiance of 30 W m^{-2} for a clear and sunny day.[49] The treatment time is therefore transformed into eqn (16.33), according to the average solar radiation Q_{UV} (W m^{-2}) received by the reactor for the sampling time interval:

$$t_{30W,i+1} = t_{w0W,i} + \left(t_{i+1} - t_i\right) \frac{Q_{UV}}{30} \left(\frac{\upsilon_R}{\upsilon_T}\right) \tag{16.33}$$

The material balance can be expressed as an equation for the reaction step at steady state, evaluated for each spatial time (τ_{pass}, the mean residence time in the reactor) as a function of the axial longitude (z). This approximation describes the dynamic behavior of the batch reactor as a finite sum of steps ($N_{Pass,Total}$) across the reactor during the total treatment time for an accumulated total energy of $Q_{UV,Total}$:[18]

$$N_{Pass,Total} = \frac{t_{Total,QUVacum,Total}}{\tau_{pass}} \tag{16.34}$$

With this approximation the mass balance can be solved in an elementary way. Coupling the material balance and the kinetic model gives the concentration of an arbitrary substrate (c_i) as a function of the axial coordinate z, for each pass through the reactor:[1]

$$c_i(z)_{\tau pass} = c_{i,\tau pass-1} \exp\left\{ 2\frac{\alpha_1}{\kappa_P} k_A^{L-H} \left(\frac{z}{\upsilon_T}\right) \int_{\upsilon_R} \frac{1}{v_z} \left[-1 + \sqrt{1 + \frac{\kappa_P}{\alpha_1} \Phi_g \hat{E}^a_{g(\lambda \to \lambda')}} \right] d\upsilon(z) \right.$$
$$\left. + k_A^{L-H} c_{i,\tau pass-1} \left(1 - \frac{c_i(z)_{\tau pass}}{c_{i,\tau pass-1}} \right) \right\} \tag{16.35}$$

The concentration at the reactor outlet corresponds to the evaluation of the function at $z = L_R$, the reactor length. Eqn (16.35) is applicable to any type of reactor and is a function of the volume integral, $\upsilon(z)$, and the OVRE, which in turn depends on the specific reactor geometry and the distribution of the

LVRPA. The material balance equation can be coupled with the material balance of the dark zone of the recirculation system, to yield a concentration ratio at the inlet and outlet of the reactor after each pass:[18]

$$c_{i,\tau\text{pass}+1} = \frac{c_i\left(t - \tau_{\text{pass}}\right)\left[\upsilon_{\text{T}} - \upsilon_{\text{R}}\right] + c_i\left(\tau_{\text{pass}}\right)\upsilon_{\text{R}}}{\upsilon_{\text{T}}} \tag{16.36}$$

For complex contaminants mixtures of pesticides, dyes, pharmaceuticals in water, the concentration (c_i) can be substituted with the total organic carbon (TOC) concentration, $C_{\text{TOC},i}$, or by the total contaminant concentration, by lumping the concentration of each contaminant into a pseudo-component.

On the other hand, the hydrodynamic model depends on the reactor type and the prevalent hydrodynamic regime. CPC and FPR reactors are usually operated under the fully developed turbulent flow regime in which viscous effects can be neglected. Table 16.7 summarizes the modeling equations for CPC and FPR reactors.[1,50–52]

Using the same methodology described above, annular photocatalytic reactors with cylindrical geometry have also been modeled.[55] The model includes the mass balance, fluid-dynamic equations, and the description of the radiation field using both the SFM and TFM. The modeling equations using dimensionless variables are shown in Table 16.8.

16.10 Thin-Film Slurry Photocatalytic Reactors

Among the different types of scalable photocatalytic reactors, thin-film slurry (TFS) photocatalytic reactors provide an excellent configuration for efficient excitation of the semiconductor photocatalyst. TFS photocatalytic reactors normally operate at higher catalyst concentrations than conventional photoreactors because of the thin reactor thickness. This property, together with the large illuminated catalytic surface area per unit volume of reactor and minimal mass transfer limitations, gives rise to a higher concentration of hydroxyl radicals generated per unit volume of reactor. Although there is simultaneously an increase in the rate of hydroxyl radical recombination, overall a TFS reactor offers a high efficiency of photon utilization, reaction rates, and reactor throughput. Such reactors are therefore suitable for industrial-scale applications of photocatalytic reactions.[51]

The most common configurations of TFS photocatalytic reactors are that of falling film or double-skin annular/flat reactors[53–55] (Figure 16.7). These reactor configurations can be operated with three different flow operation modes: falling film laminar flow, plug flow, and slit flow, which in turn can affect the performance of the photocatalytic reactor.[2,17] Falling film configurations have the advantage over double-skin annular/flat reactors of a very high mass transfer rate of the reducing agent, *i.e.*, oxygen. They also do not suffer from the filming problem of the radiation entrance wall, which occurs in photocatalytic reactors irradiated through a transparent window such as in double-skin annular/flat photocatalytic reactors. However, the latter reactor

Table 16.7 Kinetic and hydrodynamic models for solar reactors.

Reactor type	CPC reactor	FPR
Coordinate	(r,θ,z)	(x,y,z)
Reaction rate	$r_{i,(r,\theta)} = -\frac{\alpha_1}{\kappa_P}\left[-1+\sqrt{1+\frac{\kappa_P}{\alpha_1}\Phi_g\hat{E}^a_{g(\lambda\rightarrow\lambda')}(r,\theta)}\right]\theta_i^{L-H}$	$r_{i,x} = -\frac{\alpha_1}{\kappa_P}\left[-1+\sqrt{1+\frac{\kappa_P}{\alpha_1}\Phi_g\hat{E}^a_{g(\lambda\rightarrow\lambda')}(x)}\right]\theta_i^{L-H}$
Global reaction rate per surface	$\langle R_i\rangle_z = -\frac{\alpha_1}{\kappa_P}\frac{\theta_i^{L-H}}{\pi R^2}\int_r r\int_\theta\left[-1+\sqrt{1+\frac{\kappa_P}{\alpha_1}\Phi_g\hat{E}^a_{g(\lambda\rightarrow\lambda')}(r,\theta)}\right]d\theta\,dr$	$\langle R_i\rangle_z = -\frac{\alpha_1}{\kappa_P}\frac{\theta_i^{L-H}}{\delta}\int_x\left[-1+\sqrt{1+\frac{\kappa_P}{\alpha_1}\Phi_g\hat{E}^a_{g(\lambda\rightarrow\lambda')}(x)}\right]dx$
Hydrodynamic model	$\frac{v_z(r,\theta)}{v_{max}} = \left(1-\frac{r}{R}\right)^{1/\eta_z}$	$\frac{v_z(x)}{v_{max}} = \left[1-\left(\frac{x}{\delta}\right)^2\right]$
	$\eta_z = 0.41\sqrt{\frac{8}{f}}$	$v_{z,max} = \frac{1}{2}\frac{Re}{v_{z,av}}g\delta\cos\beta$
	$f = \frac{0.0076\,Re^{*0.165}}{1+Re^{*7.0}} + \frac{16}{Re}$	$\frac{v_z}{v_{z,av}} = \frac{3}{2}\left[1-\left(\frac{x}{\delta}\right)^2\right]$
	$Re^* = 3170/Re$	
	$\frac{v_z}{v_{z,av}} = \frac{(\eta_z+1)(2\eta_z+1)}{2\eta_z^2}$	$Re = \frac{\rho v_{z,av}\delta}{\mu}$

Table 16.8 Dimensionless analysis of the radiation field in annular photocatalytic reactors using suspended solid photocatalysts.[55]

Parameter	Expression
Dimensionless geometrical parameters	$a = H/L;\ \beta = L/\eta R$
Reynolds number	$N_{Re} = \dfrac{2R(1-\eta)v_z^{average}}{\nu} = \dfrac{2\delta v_z^{average}}{\nu}$
Dimensionless variables	$\xi^* = \dfrac{\xi}{\delta};\ r^* = \dfrac{r}{R};\ z^* = \dfrac{z}{H};\ (\text{LVRPA})^* = \dfrac{(\text{LVRPA})}{(\text{LVRPA})^{max}_{\xi^*=0}} = \dfrac{I_{\xi,z}}{I^{max}_{\xi^*=0}}$
Scattering albedo	$\omega = \dfrac{\sigma}{\kappa+\sigma}$
Optical thickness	$\tau = (\sigma+\kappa)c_{cat}\delta = (\sigma+\kappa)c_{cat}R(1-\eta)$
Maximum radiation intensity at surface ($\xi^* = 0$)	$I^{max}_{\xi^*=0} = f(\omega,\tau)\dfrac{r_1}{\eta R}\arctan\left(\dfrac{\beta}{2}\right)\int_{\lambda_{min}}^{\lambda_{max}} I_\lambda \,d\lambda$
Maximum LVRPA at surface ($\xi^* = 0$)	$(\text{LVRPA})^{max}_{\xi^*=0} = \kappa c_{cat} I^{max}_{\xi^*=0} = (1-\omega)\dfrac{\tau}{\delta} I^{max}_{\xi^*=0} = (1-\omega)\dfrac{\tau}{R(1-\eta)} I^{max}_{\xi^*=0}$
Dimensionless radiation intensity at inner wall ($\xi^* = 0$)	$I^*_{\xi^*=0,z^*} = \dfrac{\arctan\left[\dfrac{\beta}{2}(2az^* - a + 1)\right] - \arctan\left[\dfrac{\beta}{2}(2az^* - a - 1)\right]}{2\arctan\left(\dfrac{\beta}{2}\right)}$

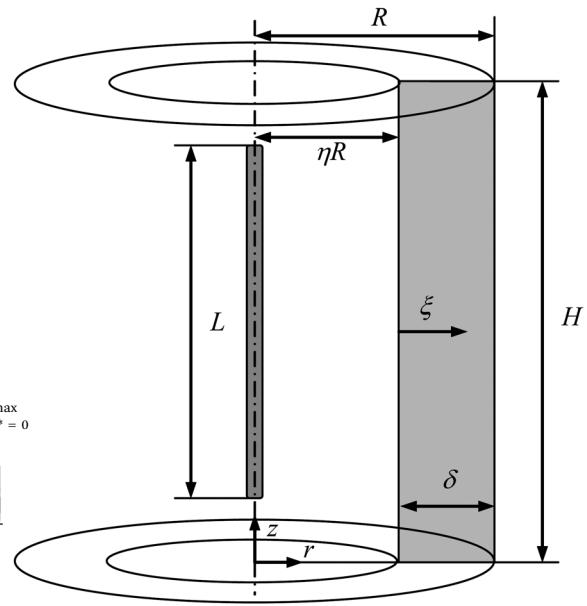

Dimensionless LVRPA and radiation model parameters	Level 1 TFS photocatalytic reactors with $\omega < 0.3$. Beer–Lambert's absorption model: $(\text{LVRPA})^* = I^*_{\xi^*=0,z^*}\exp(-\tau_{app}\xi^*)$	Level 2 TFS photocatalytic reactors, any value of ω. Two-flux absorption–scattering model: $(\text{LVRPA})^* = I^*_{\xi^*=0,z^*}\exp(-\tau_{app}\xi^*)$	Level 3 "Geometrically thick" photocatalytic reactors, any value of ω. Six-flux absorption–scattering model: $(\text{LVRPA})^* = I^*_{\xi^*=0,z^*}\dfrac{\eta}{\eta+(1-\eta)\xi^*}\exp(-\tau_{app}\xi^*)$

Apparent optical thickness

$f(\omega,\tau) = 1;$
$\tau_{app} = \tau$

$$f(\omega,\tau) = 1 + \frac{1}{\omega}\left(1 - \frac{1+\psi}{1-\psi}\sqrt{1-\omega^2}\right)$$

$$\psi = \frac{1-\sqrt{1-\omega^2}}{1+\sqrt{1-\omega^2}}\exp\left(-2\tau_{app}\right)$$

$$\tau_{app} = \tau\sqrt{1-\omega^2}$$

$$f(\omega,\tau) = \left[1 + \frac{1}{\omega_{corr}}\left(1 - \frac{1+\gamma}{1-\gamma}\sqrt{1-\omega_{corr}^2}\right)\right]\left(1 + \frac{4\omega p_s}{1-\omega p_f - \omega p_b - 2\omega p_s}\right)$$

$$a = 1 - \omega p_f - \frac{4\omega^2 p_s^2}{\left(1-\omega p_f - \omega p_b - 2\omega p_s\right)};$$

$$b = \omega p_b + \frac{4\omega^2 p_s^2}{\left(1-\omega p_f - \omega p_b - 2\omega p_s\right)}$$

$$\omega_{corr} = \frac{b}{a}; \quad \gamma = \frac{1-\sqrt{1-\omega_{corr}^2}}{1+\sqrt{1-\omega_{corr}^2}}\exp\left(-2\tau_{app}\right)$$

$$\tau_{app} = a\tau\sqrt{1-\omega_{corr}^2}$$

Absorbed radiant power

$$W_{abs} = 2\pi A_{m=1} H\eta R\left[1 - \exp\left(-\tau_{app}\right)\right] I_{\zeta^*=0}^{max}\left(1-\omega\right)\frac{\tau}{\tau_{app}}$$

$$A_{m=1} = \beta\left(a+1\right)\arctan\left[\frac{\beta}{2}\left(a+1\right)\right] - \beta\left(a-1\right)\arctan\left[\frac{\beta}{2}\left(a-1\right)\right] + \ln\frac{1+\left[\frac{\beta}{2}\left(a-1\right)\right]^2}{1+\left[\frac{\beta}{2}\left(a+1\right)\right]^2}\left[2a\beta\arctan\left(\frac{\beta}{2}\right)\right]^{-1}$$

Radiation transmission factor

$$\Psi = \frac{W_{abs}}{W_{lamp}} = \frac{2}{\pi}A_{m=1}a\left[1 - \exp\left(-\tau_{app}\right)\right]\arctan\left(\frac{\beta}{2}\right)\left(1-\omega\right)f(\omega,\tau)\frac{\tau}{\tau_{app}}$$

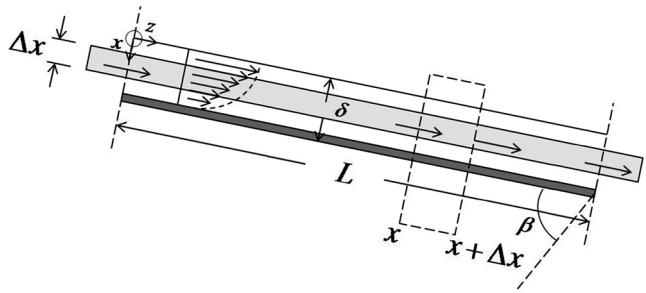

Figure 16.7 Thin film slurry photoreactors.

configurations are preferred when the solutions to be detoxified contain high concentrations of volatile organic carbons (VOCs), which may easily escape falling film reactors. Li Puma and Yue (2003)[55] have provided a methodology to design falling film and double-skin photoreactors.

16.11 Kinetic Parameters Optimization

From the material balance equation and using the same assumptions for the solution of the equation at a steady state, the function used to calculate the kinetic parameters is given by the following expression:[1]

$$\ln\left(\frac{c_i\left(t_{30\mathrm{W}}\right)}{c_{i,0}}\right) = 2\frac{\alpha_1}{\kappa_\mathrm{P}}k_\mathrm{A}^{\mathrm{L\text{-}H}}\left(\frac{t_{30\mathrm{W},i}}{\upsilon_\mathrm{T}}\right)\int_{\upsilon_\mathrm{R}}\left[-1+\sqrt{1+\frac{\kappa_\mathrm{P}}{\alpha_1}\Phi_\mathrm{g}\hat{E}^{\mathrm{a}}_{\mathrm{g}(\lambda\to\lambda')}}\right]\mathrm{d}\upsilon(z) + k_\mathrm{A}^{\mathrm{L\text{-}H}}c_{i,0}\left(1-\frac{c_i\left(t_{30\mathrm{W}}\right)}{c_{i,0}}\right) \tag{16.37}$$

A discrepancy function $F(\alpha_1, k_\mathrm{A}^{\mathrm{L\text{-}H}})$ was formulated with the following form:

$$F\left(\alpha_1, k_\mathrm{A}^{\mathrm{L\text{-}H}}\right) = \sum_{i=1}^{N\,\mathrm{data}}\left[\ln\varsigma_i - \gamma_\mathrm{kin}\Gamma_i - \beta_\mathrm{kin}g_i\right]^2 \tag{16.38}$$

$$\varsigma_i = c_i(t_{30\mathrm{W}})/c_{i,0} \tag{16.39}$$

$$\gamma_\mathrm{kin} = 2\frac{\alpha_1}{\kappa_\mathrm{P}}k_\mathrm{A}^{\mathrm{L\text{-}H}}\left(\frac{\tau_\mathrm{pass}}{\upsilon_T}\right)\int_{\upsilon_\mathrm{R}}\left[-1+\sqrt{1+\frac{\kappa_\mathrm{P}}{\alpha_1}\Phi_\mathrm{g}\hat{E}^{\mathrm{a}}_{\mathrm{g}(\lambda\to\lambda')}}\right]\mathrm{d}\upsilon(z) \tag{16.40}$$

$$\Gamma_i = t_{30\mathrm{W}}/\tau_\mathrm{pass} \tag{16.41}$$

$$\beta_\mathrm{kin} = k_\mathrm{A}^{\mathrm{L\text{-}H}}c_{i,0} \tag{16.42}$$

$$g_i = 1 - \varsigma_i \tag{16.43}$$

Applying the method of least-squares to the discrepancy function (eqn (16.38)), the following residual functions, ζ_1, ζ_2, were obtained to determine the parameters:[1]

$$\zeta_1\left(\alpha_1, k_{\mathrm{A}}^{\mathrm{L-H}}\right) = \frac{\partial F}{\partial \alpha_1} = \sum_{i=1}^{N\,\mathrm{data}} \left[\left(\ln \varsigma_i - \gamma_{\mathrm{kin}} \Gamma_i - \beta_{\mathrm{kin}} g_i\right) \Gamma_i\right] = 0 \tag{16.44}$$

$$\zeta_2\left(\alpha_1, k_{\mathrm{A}}^{\mathrm{L-H}}\right) = \frac{\partial F}{\partial k_{\mathrm{A}}^{\mathrm{L-H}}} = \sum_{i=1}^{N\,\mathrm{data}} \left[\left(\ln \varsigma_i - \gamma_{\mathrm{kin}} \Gamma_i - \beta_{\mathrm{kin}} g_i\right)\left(\Gamma_i \frac{\partial \gamma_{\mathrm{kin}}}{\partial k_{\mathrm{A}}^{\mathrm{L-H}}} + g_i \frac{\beta_{\mathrm{kin}}}{k_{\mathrm{A}}^{\mathrm{L-H}}}\right)\right] = 0 \tag{16.45}$$

The solution to the equation system is given by:

$$\begin{bmatrix} \dfrac{\partial \zeta_1}{\partial \alpha_1} & \dfrac{\partial \zeta_1}{\partial k_{\mathrm{A}}^{\mathrm{L-H}}} \\ \dfrac{\partial \zeta_2}{\partial \alpha_1} & \dfrac{\partial \zeta_2}{\partial k_{\mathrm{A}}^{\mathrm{L-H}}} \end{bmatrix}^{(m)} \times \begin{bmatrix} \Delta \alpha_1^{(m)} \\ \Delta k_{\mathrm{A}}^{\mathrm{L-H}(m)} \end{bmatrix} = \begin{bmatrix} \zeta_1^{(m)} \\ \zeta_2^{(m)} \end{bmatrix} \tag{16.46}$$

$$\alpha_1^{(m+1)} = \alpha_1^{(m)} + \lambda^{\cdot} \Delta \alpha_1^{(m)} \tag{16.47}$$

$$k_{\mathrm{A}}^{\mathrm{L-H}(m+1)} = k_{\mathrm{A}}^{\mathrm{L-H}(m)} + \lambda^{\cdot} \Delta k_{\mathrm{A}}^{\mathrm{L-H}(m)} \tag{16.48}$$

where the matrix corresponds to the Jacobian of the residual functions; $\Delta \alpha_1^{(m)}$, $\Delta k_{\mathrm{A}}^{\mathrm{L-H}(m)}$ represent the linear solutions for the mth iteration; $\lambda^{\cdot}$ is a variational damping coefficient of the Broyden type, a function of the Euclidean norm $\|N\|$ of the discrepancy functions ζ_1, ζ_2 and constrained by the following conditions:[56]

$$\lambda^{\cdot} = 1 \quad (\|N\| < 1) \tag{16.49}$$

$$\lambda^{\cdot} = \frac{-1 + \sqrt{1 + 6\|N\|}}{3\|N\|} \quad \|N\| > 1 \tag{16.50}$$

$$\|N\| = \frac{\sqrt{\zeta_1^{2(m+1)} + \zeta_2^{2(m+1)}}}{\sqrt{\zeta_1^{2(m)} + \zeta_2^{2(m)}}} \tag{16.51}$$

Because the kinetic parameter appears inside the square root and because this parameter is necessarily greater than zero, the solution above can be constrained by the following additional condition:

$$1 + \frac{\kappa_{\mathrm{P}}}{\alpha_1} \Phi_{\mathrm{g}} \hat{E}^{\mathrm{a}}_{\mathrm{g}(\lambda \to \lambda')} \geq 0 \tag{16.52}$$

The above solution ensures convergence, involves low computational times on a PC (<1 s) and shows high accuracy in predicting the experimental data. The same approach was used for the solution of the material balance equation at steady-state in terms of the axial coordinate z during each pass through the reactor.

16.12 Application of Models to the Photocatalytic Degradation of Organic Compounds in Water

The models presented in the early sections were validated in four different solar, pilot-scale photocatalytic reactors located at the Solar Platform of Universidad del Valle, Cali, Colombia (3° 30′ North latitude). Three CPC reactors were used, which had different surface areas but the same design configuration (henceforth called CPC-I, CPC-II, and CPC-III) and a flat plate, falling film reactor (FPR). The compounds degraded were dichloroacetic acid (DCA), 4-chlorophenol (4-CP), and analytical grade phenol (PH). Binary 2 : 1 molar proportions and ternary 1 : 1 : 1 mixtures of these compounds were tested in the reactor to demonstrate the robustness of the models. The CPC-I reactor and experimental procedures were the same as those in Colina-Márquez, Machuca-Martínez, and Li Puma.[18] The experimental tests were conducted between March and September, 2011, and between February and March, 2012. Table 16.9 shows the reactor's specifications.[1]

The experiments were performed in a random fashion in different reactors under different operating conditions using the same total volume of liquid. The total initial concentration of contaminants was 120, 60, or 30 ppm and the catalyst loading was 0.1, 0.35, or 1.0 g cm^{-3}. The initial pH was adjusted to 3.5 using phosphoric acid in all experiments. The reactors were operated in recirculation mode with a total volume of 20 (FPR), 30 (CPC-I), 50 (CPC-II), and 70 L (CPC-III) with flow rates of 75 (FPR), 80 (CPC-I) and 95 L min^{-1} (CPC CPC-II and-III), 90% oxygen saturation and at a water temperature of 31.0 ± 2.5 °C.

Table 16.9 Photoreactor's specifications.

Reactors	CPC-I (ref. 1)	FPR
Material reactor	Duran glass (ten tubes)	Borosilicate glass
Diameter	32 mm (o.d.)	—
Thickness (mm)	1.4 (wall)	5 (flat)
Length (mm)	CPC-I, 1200 (by tube); CPC-II, 2400; CPC-III, 3600	128 (flat)
Width (mm)	—	98 (flat)
Thickness film (mm)	—	2 (film of slurry)
Inclination angle (°)	—	3.5
Reaction volume, υ_R (L)	CPC-I, 10.0; CPC-II, 20.0; CPC-III, 30.0	2.5
Total volume of reactor, $\upsilon_{T,max}$ (L)	CPC-I, 40; CPC-II, 70.0; CPC-III, 120.0	25
Material reflector	Reflective aluminum	—
Involute reflector acceptance angle (°)	90	—
Reflectivity	0.85	—

16.12.1 DCA Solar Photodegradation

The kinetic model based on hydroxyl radical attack predicted the photodegradation of dichloroacetic acid with a high degree of confidence in both CPC-I and FPR (Figure 16.8). The kinetic parameters were obtained by fitting the model to the experimental results in the cylindrical reactor geometry (CPC-I) and further applied without correction to the flat reactor geometry (FPR). The kinetic parameters were therefore intrinsic parameters independent of the radiant field configuration and the scale of the process. Correction effects associated with the reactor geometry, catalyst loading, and scale factors are considered directly in the evaluation of the quantum yield and OVREA through the proposed mathematical model.

In another study, Sagawe *et al.* (2010)[32] directly used an L–H model modified with a global correction factor to consider the effect of the LVRPA. However, this model could not fit the degradation of DCA in the CPC-I and FPR.

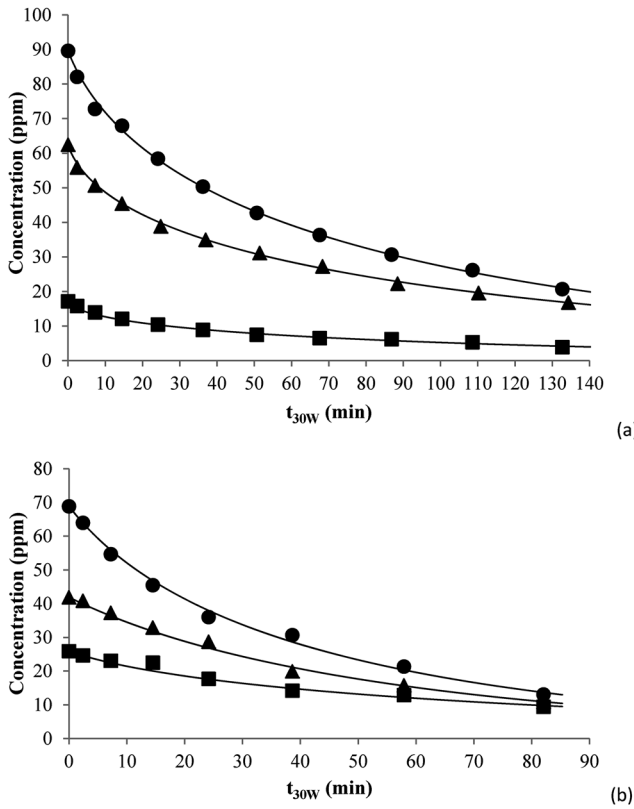

Figure 16.8 Solar photodegradation of DCA (dichloroacetic acid), experimental data and model (—) for an initial concentration of (●) 120, (▲) 60, and (■) 30 ppm and [TiO_2–P25] = 0.35 kg m^{-3}. (a) CPC-I.[1] (Adapted from Mueses *et al.*, 2013.[1] Reproduced with permission of Elsevier copyright 2015.) (b) For a flat-plate reactor (FPR).

The kinetic parameters of the model were found to be negative and therefore physically inconsistent.[57]

The FPR was found to be more effective than the CPC-I reactor in the degradation of DCA, which matches the higher values of LVRPA observed in the FPR at equal optical thicknesses, although the performance in the FPR is affected negatively by the hydrodynamic effects.

Finally, it should be observed that the solar photodegradation experimental results differ significantly from those reported in the literature, under the same operating conditions, in laboratory-scale reactors irradiated by UV lamps,[58,59] implying that laboratory data may not be the most suitable for scaling photocatalytic reactors to the solar scale, because of the different LVRPA distribution observed.

16.12.2 Phenol and 4-Chlorophenol Solar Photodegradation

The kinetics of photodegradation of phenol have been commonly described with the L–H kinetic model, with satisfactory results for predictions under different operating conditions.[23,26,29,36]

The empirical direct–indirect model[26] by Salvador *et al.*, differs from the L–H model. This model considers the attack of photogenerated holes on the pollutant molecules absorbed on the TiO_2 surface, arguing against the possibility of photo-oxidation of water. Although the Salvador model is theoretically acceptable, the model can only be applied to a limited number of photocatalytic reactions. Furthermore, the model has three adjustable parameters and is therefore not comparable to the simpler predictive capability of the L–H kinetic model. Sagawe *et al.* (2010)[32] proposed an empirical modification of the model given by Ollis. However, this model could not predict the behavior of the photodegradation of phenol at high contaminant concentrations, even when the effect of photonic correction was considered.

Figure 16.9 shows the experimental data and the authors' model predictions for the solar photodegradation of phenol in three CPC reactors. The predictive capability of the model shown in this chapter allows a satisfactory description of the photodegradation of phenol even at higher initial concentrations. This behavior is associated with the correction effect of the variation in the quantum yields and the radiant field configuration due to optical effects and catalyst loading. The proposed model can be generalized to any scale and operating conditions.

The behaviors obtained show the greater effect of the projected area of reactor exposed to solar radiation. The CPC-III reactor, with three times the area of reactor I, achieved a higher percentage of phenol degradation at the same standardized treatment time.

Similarly the degradation of 4-chlorophenol was well represented by the model presented here (Figure 16.10) but not by the L–H model,[33] which was not suitable at higher concentrations of 4-chlorophenol.

The photodegradation of 4-CP follows an apparent first-order kinetics.[58] Satuf *et al.* (2007)[59] therefore proposed a first-order model with an explicit

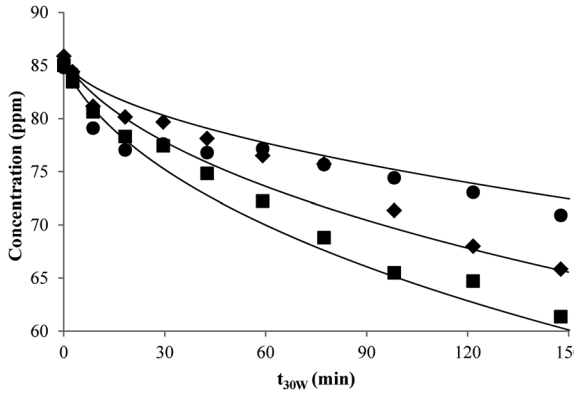

Figure 16.9 Performance of experimental data and model (▬) in solar photodegradation of phenol using CPC-I (●), II (◆), and III (■) with $[TiO_2] = 0.1$ kg m^{-3}, $c_{i,0} = 120$ ppm on a sunny day; $\omega = 0.88$, $\kappa = 174.749$ m^2 kg^{-1} and $\sigma = 1274.74$ m^2 kg^{-1}. (Adapted from Mueses *et al.*, 2013.[1] Reproduced with permission of Elsevier copyright 2015.)

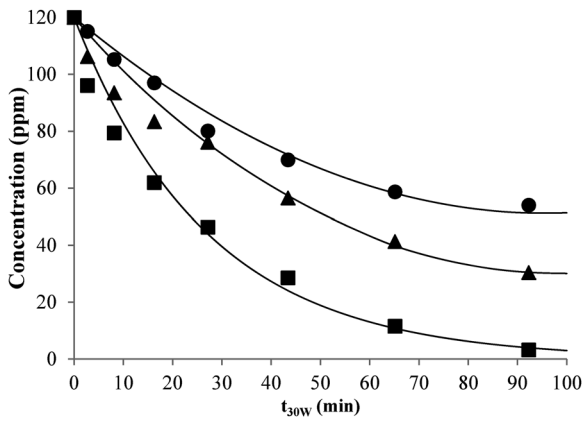

Figure 16.10 Performance of experimental data and model (▬) in solar photodegradation of 4-chlorophenol using CPC-I (●), II (◆), and III (■) with $[TiO_2] = 0.5$ kg m^{-3}, $c_{i,0} = 120$ ppm on a sunny day; $\omega = 0.88$, $\kappa = 174.749$ m^2 kg^{-1} and $\sigma = 1274.74$ m^2 kg^{-1}. (Adapted from Mueses *et al.*, 2013.[1] Reproduced with permission of Elsevier copyright 2015.)

dependence on the light output and based on the same hydroxyl radical attack mechanism used in this work. They obtained the same simplified mathematical structure as for case IV of the generalized model.

The degradation of 4-chlorophenol at any scale is complex due to the formation of intermediate substances such as 4-chlorocatecol, benzoquinone, and hydroquinone.[59] These intermediates affect the overall efficiency of the mineralization process. At the solar scale, the presence of these transformation

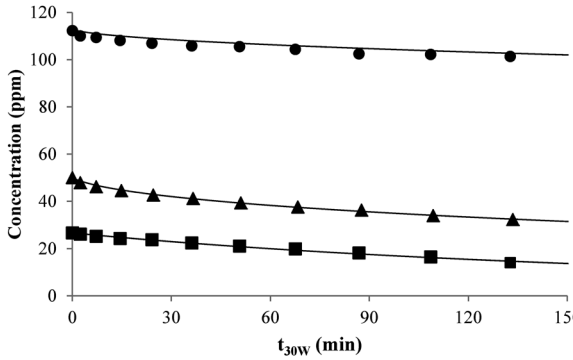

Figure 16.11 Phenol photodegradation with a low catalyst concentration (0.05 kg m^{-3}) and different initial concentrations: (●) 120, (▲) 60, and (■) 30 ppm. Model (▬). (Adapted from Mueses *et al.*, 2013.[1] Reproduced with permission of Elsevier copyright 2015.)

products was detected by observing a color change of the water. However, despite the presence of intermediates, the performance of the overall photodegradation of phenol could be modeled without considering the effects of transformation products. The predictions of the experimental data measured by TOC corroborated with the chloride ion measurements. As for phenol degradation, the CPC-III reactor achieved better performance for the same treatment time.

For phenol at low concentrations of catalyst, the radiant field effects were negligible. In this case, the proposed model was reduced to a conventional L–H model with a global constant that screened the effect of the luminous flux, enabling it to also be applied to high reagent concentrations. Figure 16.11 presents experimental data and the model for the CPC-I reactor with a catalyst load of 0.1 g L^{-1} of TiO_2.

16.13 Photodegradation of Organic Mixtures

The model was also applied to binary and ternary mixtures of the compounds investigated. The model predicted the solar scale photodegradation of these mixtures (see Figures 16.12–16.15), further validating the model.

Figure 16.14 shows experimental data on a sunny day and simulations in the FPR for: M×2 (◆): DCA + 4-CP (1 : 2) with $c_{i,0}$ = 50 ppm, pH 4.3 and C_{Cat} = 0.35 g L^{-1}; M×3 (■): PH + DCA (2 : 1) with $c_{i,0}$ = 50 ppm, pH 3.5 and C_{Cat} = 0.35 g L^{-1}; M×4 (▲): 4CP + PH (2 : 1) with $c_{i,0}$ = 75 ppm, pH 4.0 and C_{Cat} = 0.2 g L^{-1}; and M×5 (●): DCA + 4CP + PH (1 : 1 : 1) with $c_{i,0}$ = 60 ppm, pH 4.0 and C_{Cat} = 0.1 g L^{-1}.

The model was also applied in the predictions of solar photodegradation of a mixture of pesticides reported by Colina-Márquez, Machuca-Martínez, and Li Puma (2009) in CPC-I with $I_{average}$ = 10.0 W m^{-2}, [TiO_2] = 0.6 g L^{-1}, and pH 9 (Figure 16.15).[18]

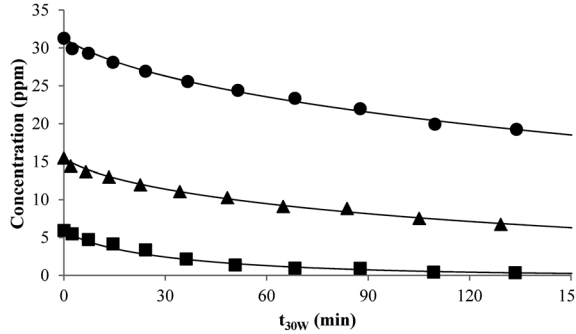

Figure 16.12 Solar photodegradation of mixture 1, M×1: DCA + 4-CP (2 : 1) applied to (●) 120, (▲) 60, and (■) 30 ppm, and (▬) model with $[TiO_2] = 0.35$ kg m^{-3} in CPC-I. (Adapted from Mueses *et al.*, 2013.[1] Reproduced with permission of Elsevier copyright 2015.)

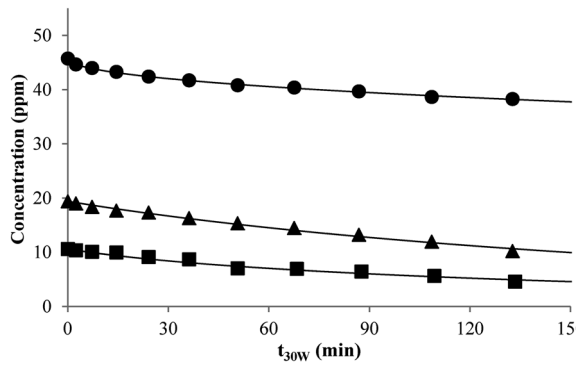

Figure 16.13 Solar photodegradation of mixture 2, M×2: DCA + 4-CP (1 : 2) applied to (●) 120, (▲) 60, and (■) 30 ppm, and (▬) model with $[TiO_2] = 0.35$ kg m^{-3} in CPC-I. (Adapted from Mueses *et al.*, 2013.[1] Reproduced with permission of Elsevier copyright 2015.)

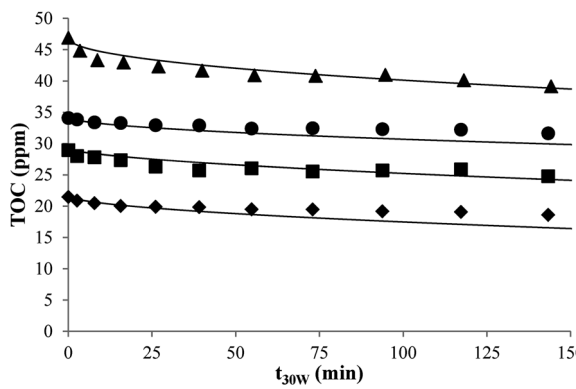

Figure 16.14 Solar photodegradation of M×2 (◆), M×3 (■), M×4 (▲), and M×5 (●) and proposed model (—) in a flat-plate reactor (FPR) (TOC, total organic carbon) (see text for details).

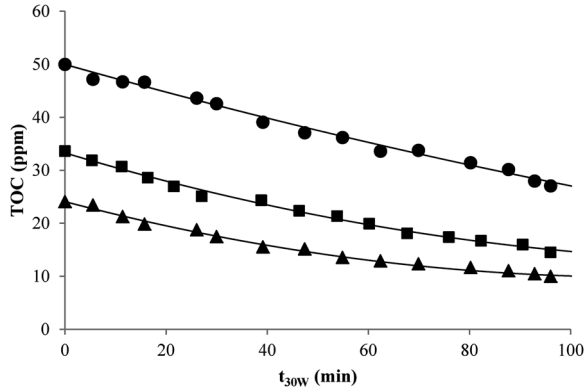

Figure 16.15 Solar photodegradation of a pesticide mixture with a commercial formulation of 2,4-D (2,4-dichlorophenoxy-acetic acid), diuron, and Ametryne: (●) 50, (■) 35, and (▲) 25 ppm (TOC, total organic carbon) (see text for details).

References

1. M. A. Mueses, F. Machuca-Martínez and G. Li Puma, Effective quantum yield and reaction rate model for evaluation of photocatalytic degradation of water contaminants in heterogeneous pilot-scale solar photoreactors, *Chem. Eng. J.*, 2013, **215**, 937–947.
2. G. Li Puma and A. Brucato, Dimensionless analysis of slurry photocatalytic reactors using two-flux and six-flux absorption–scattering models, *Catal. Today*, 2007, **122**, 78–90.
3. A. Cassano and O. Alfano, Reaction engineering of suspended solid heterogeneous photocatalytic reactors, *Catal. Today*, 2000, **58**, 167–197.
4. IDEAM, *Atlas De Radiación Solar De Colombia-2005, Ministerio del Medio Ambiente: Bogotá (Colombia). Obtenido de IDEAM*, 2012, https://documentacion.ideam.gov.co/openbiblio/Bvirtual/019649/019649.htm.
5. S. Spadoni, C. Stramigioli and F. Santarelli, Rigorous and simplified approach to the modelling of continuous photoreactors, *Chem. Eng. Sci.*, 1980, **35**, 935.
6. C. Martin, M. Baltanas and A. Cassano, Photocatalytic reactors II. Quantum efficiencies allowing for scattering effects. An experimental approximation, *J. Photochem. Photobiol., A*, 1996, **94**, 173–189.
7. A. Brucato and L. Rizzuti, Simplified modeling of radiant fields in heterogeneous photoreactors. 1. Case of zero reflectance, *Ind. Eng. Chem. Res.*, 1997, **36**, 4740–4747.
8. A. Brucato and L. Rizzuti, Simplified modeling of radiant fields in heterogeneous photoreactors. 2 Limiting two flux model for the case of reflectance greater than zero, *Ind. Eng. Chem. Res.*, 1997, **36**, 4748–4755.
9. G. Li Puma, J. Khor and A. Brucato, Modeling of an annular photocatalytic reactor for water purification: oxidation of pesticides, *Environ. Sci. Technol.*, 2004, **38**, 3737–3745.

10. M. Satuf, R. Brandi, A. Cassano and O. Alfano, Experimental method to evaluate the optical properties of aqueous titanium dioxide suspensions, *Ind. Eng. Res.*, 2005, **44**, 6643–6649.
11. M. Peterson, J. Turner and A. Nozik, Mechanistic studies of the photocatalytic behavior of TiO_2 particles in a photoelectrochemical slurry cell and the relevance to photodetoxification reactions, *J. Phys. Chem.*, 1991, **95**, 221–225.
12. A. Brucato, A. Cassano, F. Grisafi, G. Montante, L. Rizzuti and G. Vella, Estimating radiant fields in flat heterogeneous photoreactors by the six-flux model, *AIChE J.*, 2006, **52**, 3882–3890.
13. M. Satuf, R. Brandi, A. Cassano and O. Alfano, An experimental method to evaluate the optical properties of aqueous titanium dioxide suspensions, *Ind. Eng. Chem. Res.*, 2005, **44**, 6643–6649.
14. G. Raupp, J. Nico, S. Annangi, R. Changrani and R. Annapragada, Two-flux radiation-filed model for an annular packed-bed photocatalytic oxidation reactor, *AIChE J.*, 1997, **43**, 792–801.
15. M. Pasquali, F. Santarelli, J. Porter and P. Yue, Radiative transfer in photocatalytic systems, *AIChE J.*, 1996, **42**, 532–536.
16. H. Otálvaro-Marín, M. Mueses and F. Machuca-Martínez, Boundary layer of photon absorption applied to heterogeneous photocatalytic solar flat plate reactor design, *Int. J. Photoenergy*, 2014, 1–9.
17. G. Li Puma, Dimensionless analysis of photocatalytic reactors using suspended solid photocatalysts, *Chem. Eng. Res. Des.*, 2005, **83**, 820–826.
18. J. Colina-Márquez, F. Machuca-Martínez and G. Li Puma, Photocatalytic mineralization of commercial herbicides in a pilot-scale solar CPC reactor: photoreactor modeling and reaction kinetics constants independent of radiation field, *Environ. Sci. Technol.*, 2009, **43**, 8953–8960.
19. R. Brandi, O. Alfano and E. Cassano, Rigorous model and experimental verification of the radiation field in a flat-plate solar collector simulator employed for photocatalytic reactions, *Chem. Eng. Sci.*, 1999, **54**, 2817–2827.
20. N. Serpone, Relative photonic efficiencies and quantum yields in heterogeneous photocatalysis, *J. Photochem. Photobiol., A*, 1997, **104**, 1–12.
21. D. Friedmann, C. Mendive and D. Bahnemann, TiO_2 for water treatment: parameters affecting the kinetics and mechanism of photocatalysis, *Appl. Catal., B*, 2010, **99**, 398–406.
22. J. Herrmann, Fundamentals and misconceptions in photocatalysis, *J. Photochem. Photobiol., A*, 2010, **216**, 85–93.
23. D. Monllor-Satoca, R. Gómez, M. González-Hidalgo and P. Salvador, The Direct-Indirect model: an alternative kinetic approach in heterogeneous photocatalysis base on the degree of interaction of dissolved pollutant species with the semiconductor surface, *Catal. Today*, 2007, **129**, 247–255.
24. O. Alfano, M. Cabrera and A. Cassano, Photocatalytic reaction involving hydroxyl radical attack I: reaction kinetic formulation with explicit photon absorption effects, *J. Catal.*, 1997, **172**, 370–379.

25. C. Turchi and D. Ollis, Photocatalytic degradation of organic water contaminants: mechanisms involving hyroxyl radical attack, *J. Catal.*, 1990, **122**, 178–192.
26. T. Lana-Villarreal, R. Gómez, M. Gonzalez and P. Salvador, A kinetic model of distinguishing between direct and indirect interfacial hole transfer in heterogeneous photooxidation of dissolved organics on TiO_2 nanoparticle suspensions, *J. Phys. Chem. B*, 2004, **108**, 20278–20290.
27. A. Fujishima, X. Zhang and D. Tryk, TiO_2 photocatalysis and related surface phenomena, *Surf. Sci. Rep.*, 2008, **63**, 515–582.
28. A. Mills, J. Wang and D. Ollis, Kinetic of liquid phase semiconductor photoassisted reactions: supporting observations for a pseudo-steady state model, *J. Phys. Chem. B*, 2006, **110**, 14386–14390.
29. D. Ollis, Kinetics of liquid phase photocatalyzed reactions: an illuminating approach, *J. Phys. Chem. B*, 2005, **109**, 2439–2444.
30. A. Linsebigler, G. Lu and T. Yates, Photocatalysis on TiO_2 surfaces: principles mechanisms, and select results, *Chem. Rev.*, 1995, **95**, 735–758.
31. B. Hammer, S. Wendt and F. Besenbacher, Water Absortion on TiO_2, *Top. Catal.*, 2010, **53**, 423–430.
32. G. Sagawe, M. Satuf, R. Brandi, J. Muschner, C. Federer, O. Alfano and Otros, Analysis of photocatalytic reactors employing the photonic efficiency and removal efficiency parameters: degradation of radiation absorbing and nonabsorbing pollutants, *Ind. Eng. Chem. Res.*, 2010, **49**, 6898–6908.
33. M. Satuf, R. Brandi, A. Cassano and O. Alfano, Scaling-up of slurry reactors for the photocatalytic degradation of 4-chlorophenol, *Catal. Today*, 2007, **129**, 110–117.
34. C. Zalazar, R. Romero, C. Martin and A. Cassano, Photocatalytic intrinsic reaction kinetics I: mineralization of dichloroacetic acid, *Chem. Eng. Sci.*, 2005, **60**, 5240–5254.
35. S. Valencia, F. Cataño, L. Rios, G. Restrepo and J. Marín, A new kinetic model for heterogeneous photocatalysis with titanium dioxide: case non-specific absorption considering back reaction, *Appl. Catal., B*, 2011, **104**, 300–304.
36. J. Montoya, A. Velásquez and P. Salvador, The direct-indirect kinetic model in photocatalyis: a reanalysis of phenol and formic acid degradation rate dependence of photon flow and concentration in TiO_2 aqueous dispersions, *Appl. Catal., B*, 2009, **88**, 50–58.
37. M. Ballari, O. Alfano and A. Cassano, Photocatalytic degradation of dichloroacetic acid. A kinetic study with a mechanistically based reaction model, *Ind. Eng. Chem. Res.*, 2009, **48**, 1847–1858.
38. M. Cabrera, A. Negro, O. Alfano and A. Cassano, Photocatalytic reactions involving hydroxyl radical attack II. Kinetics of the decomposition of trichloroethylene using titanium dioxide, *J. Catal.*, 1997, **172**, 380–390.
39. D. Bahanemman, M. Hilgendorff and R. Memming, Charge carrier dynamics at TiO2 particles: reactivity of free and trapped holes, *J. Phys. Chem. B*, 1997, **101**, 4265–4275.
40. R. Brandi, J. Citroni, O. Alfano and A. Cassano, Absolute quantum yields in photocatalytic slurry reactor, *Chem. Eng. Sci.*, 2003, **58**, 979–985.

41. S. Ahmed, M. Rasul, R. Brown and M. Hashib, Influence of parameters of the heterogeneous photocatalytic degradation of pesticides and phenolic contaminants in wastewater: a short review, *J. Environ. Manage.*, 2011, **92**, 311–330.
42. B. Liu, N. Kazuya, X. Zhao, T. Ochiai, T. Murakami and A. Fujishima, Theoretical kinetic analysis of heterogeneous photocatalysis: the effects of surface trapping and bulk recombination through defects, *J. Phys. Chem. C*, 2011, **115**, 16037–16042.
43. G. Li Puma, V. Puddu, H. Tsang, A. Gora and B. Toepfer, Photocatalytic oxidation of multicomponent mixtures of estrogens (estrone (E1), 17β-estradiol (E2), 17α-ethynylestradiol (EE2) and estriol (E3)) under UVA and UVC radiation: photon absorption, quantum yields and rate constants independent of photon absorption, *Appl. Catal., B*, 2010, **99**, 388–397.
44. F. Machuca-Martínez, J. Colina-Márquez and M. Mueses, Determination of quantum yield in a heterogeneous photocatalytic system using a fitting-parameters model, *J. Adv. Oxid. Technol.*, 2008, **11**, 42–48.
45. J. Colina-Márquez, F. Machuca-Martínez and G. Li Puma, Radiation absorption and optimization of solar photocatalytic reactors for environmental applications, *Environ. Sci. Technol.*, 2010, **44**, 5112–5120.
46. N. Serpone and A. Emeline, Semiconductor photocatalysis: past, present and future outlook, *J. Phys. Chem. Lett.*, 2012, **3**, 673–677.
47. T. Bandosz, J. Jagiello, C. Contescu and J. Schwarz, Characterization of the surfaces of activated carbons in terms of their acid constant distribution, *Carbon*, 1993, **31**, 1193–1202.
48. N. Bundalesky, A. Silva, U. Schoröder, A. Moutinho and O. Teodoro, Adsorption dynamics of water on the surface on TiO2(110), *J. Phys.: Conf. Ser.*, 2010, **257**, 012008.
49. S. Malato, P. Fernández, M. Maldonado, J. Blanco and W. Gernjak, Decontamination and disinfection of water by solar photocatalysis: recent overview and trends, *Catal. Today*, 2009, **147**, 1–59.
50. G. Camera-Roda and F. Santarelli, A radiation approach to the design of photocatalytic reactor, *Ind. Eng. Chem. Res.*, 2007, **46**, 7637–7644.
51. M. A. Mueses, F. Machuca-Martinez, A. Hernández-Ramirez and G. Li Puma, Effective radiation field model to scattering - absorption applied in heterogeneous photocatalytic reactors, *Chem. Eng. J.*, 2015, **279**, 442–451.
52. E. Romeo, C. Royo and A. Monzón, Improved explicit equations for estimation of the friction factor in rough and smooth pipes, *Chem. Eng. J.*, 2002, **86**, 369–374.
53. G. Li Puma and P. Yue, Comparison of the effectiveness of photon-based oxidation processes in a pilot falling film photoreactor, *Environ. Sci. Technol.*, 1999, **33**, 3210–3216.
54. O. Alfano, D. Bahnemann, A. Cassano, R. Dillert and R. Goslich, Photocatalysis in water environments using artificial and solar light, *Catal. Today*, 2000, **58**, 199–230.
55. G. Li Puma and P. Yue, Modelling and design of thin-film slurry photocatalytic reactors for water purification, *Chem. Eng. Sci.*, 2003, **58**, 2269–2281.

56. M. Mueses and F. Machuca-Martínez, Una Solución de la Ecuación de Rachford-Rice para Sistemas Multifases Aplicando el Método Newton-Raphson, un Parámetro de Broyden y el Flash Negativo, *Inf. Tecnol.*, 2010, **21**, 3–10.
57. M. Mueses, J. Colina and F. Machuca, Degradación fotocatalítica de ácido dicloroacético al aplicar un campo de radiación de baja energía, *Ing. Desarrollo*, 2008, **24**, 33–47.
58. M. Satuf, R. Brandi, A. Cassano and O. Alfano, Photocatalytic degradation of 4-chlorophenol: a kinetic study, *Appl. Catal., B*, 2008, **82**, 37–49.
59. M. Satuf, R. Brandi, A. Cassano and O. Alfano, Quantum efficiencies of 4-chlorophenol photocatalytic degradation and mineralization in a well-mixed slurry reactor, *Ind. Eng. Chem. Res.*, 2007, **46**, 43–51.